FABRICATION, STRUCTURE, AND TRANSPORT PROPERTIES OF NANOWIRES

Yu-Ming Lin,[1] Mildred S. Dresselhaus,[1,2] and Jackie Y. Ying[3]*

[1]Department of Electrical Engineering and Computer Science, [2]Department of Physics, and [3]Department of Chemical Engineering, Massachusetts Institute of Technology, Cambridge Massachusetts 02139

Nanowire systems have attracted a great deal of attention recently due to their technological potential. They are of fundamental interest because they exhibit unique quantum confinement effects. In this article, advances in the fabrication of nanowires via template-assisted and laser-assisted approaches are reviewed. The structure and characteristics of different nanowire systems are discussed. To understand and predict the unusual properties of nanowires, we have developed a generalized theoretical model for the band structure of these one-dimensional systems. A unique semimetal–semiconductor transition that occurs in bismuth nanowires is described. Transport measurements on bismuth and antimony nanowires illustrate that these novel materials are very different from their bulk counterparts. A transport

* To whom correspondence should be addressed.

ADVANCES IN CHEMICAL ENGINEERING, VOL. 27 0065-2377/01 $35.00

model, based on the band-structure calculations, is presented to explain the experimental results and to gain insight into the transport phenomena of nanowire systems.

I. Introduction

Nanostructured materials have received significant attention in recent years because of their fundamental importance and potential applications in areas ranging from chemistry, physics, biology, and materials science. In the fields of electronics and optics, the drive to miniaturize devices and increase storage density has fueled research in nanotechnology. Several techniques have been developed to fabricate nanostructures, such as epitaxial growth, electron beam lithography, chemical vapor deposition, and self-assembly approaches. Nanostructures represent a new class of materials with properties different from molecular species and bulk solid-state structures. They exhibit quantum confinement effects, giving rise to unique behavior that can be exploited in novel optical, magnetic, electronic, and thermoelectric devices. Multiple quantum well structures are probably the most studied nanostructured systems; the carriers are confined to two dimensions in these systems. In comparison, one-dimensional quantum wires and zero-dimensional quantum dots are expected to show even stronger quantum confinement effects. Quantum wires are perhaps the most amenable for the design of novel electronic devices because they exhibit more pronounced quantum effects than the two-dimensional structures; unlike most zero-dimensional systems, they maintain transport continuity along the wire axis. This chapter describes the fabrication, structure, and transport properties of nanowire systems of interest to electronic applications. It presents a generalized theoretical model for the band structure of quantum wires, which is responsible for the novel behavior of these systems. In addition, a semiclassical transport model is also developed so that the unusual transport properties that are experimentally observed in nanowire systems can be explained and compared to the predicted behavior.

II. Fabrication and Structural Characteristics of Nanowires

The preparation of one-dimensional quantum systems represents one of the greatest challenges in materials fabrication. The synthesis of highly crystalline and continuous nanowires is essential for studying the interesting

quantum phenomena in these low-dimensional systems. Over the past decade, significant progress has been made in deriving nanowires via techniques, such as high-pressure injection (Huber *et al.,* 1994, 1999; Zhang *et al.,* 1998a, 1999), vapor deposition (Heremans *et al.,* 2000; Cheng *et al.,* 1999), electrochemical deposition (Foss *et al.,* 1992; Hornyak *et al.,* 1997; Fasol, 1998; Piraux *et al.,* 1994, 1999; Martin, 1994; Sun *et al.,* 1999a; Whitney *et al.,* 1993; Blondel *et al.,* 1994; Liu *et al.,* 1998a; Routkevitch *et al.,* 1996a,b; Yi and Schwarzacher, 1999; Peng *et al.,* 2000; Zeng *et al.,* 2000), laser ablation (Morales and Lieber, 1998; Yu *et al.,* 1998; Zhang *et al.,* 1998b, 2000a; Duan *et al.,* 2000), thermal evaporation (Wang *et al.,* 1998a; Tang *et al.,* 1999), molecular beam epitaxy (Nötzel *et al.,* 1992; Omi and Ogino, 1997), and electron beam lithography (Chou *et al.,* 1996). These different methods led to the generation of a broad range of one-dimensional nanostructured materials (Martin, 1994). Although some approaches are more suitable than others for specific applications, each approach may present certain synthetic limitations with regard to nanowire diameter, crystallinity, fabrication costs, and scalability. In this section, the nanowire-fabrication techniques will be reviewed, and the structure of the nanowires produced will be discussed.

A. Template-Assisted Synthesis

The template-assisted synthesis of nanowires is a conceptually elegant way of fabricating nanostructures in an organized assembly (Ozin, 1992; Tonucci *et al.,* 1992; Ying, 1999). The template is typically a nonconducting host matrix containing nanometer-sized elongated pores or voids, which are filled by the material of choice that adopts the pore morphology. If the pore diameters are sufficiently small, the pore-filling nanowires would exhibit quantum confinement effects. In this synthesis approach, the important factors for consideration include the template characteristics, such as chemical stability, mechanical properties, pore diameter, uniformity, and density. Templates that have been used for nanowire synthesis include anodic alumina, nanochannel glass, ion track-etched polymers, and mica films.

Anodic alumina templates are produced by the anodic oxidation of aluminum films in acidic electrolyte solutions (Diggle *et al.,* 1969; O'Sullivan and Wood, 1970; Li *et al.,* 1998a). The resulting aluminum oxide film possesses a regular hexagonal array of parallel and nearly cylindrical channels (Keller *et al.,* 1953; Masuda *et al.,* 1997; Li *et al.,* 1998a), as depicted in Fig. 1. Depending on the anodization conditions, such as the voltage applied and the nature and concentration of electrolyte used, the pores of anodic alumina can be systematically varied from less than 10 nm to 200 nm in diameter,

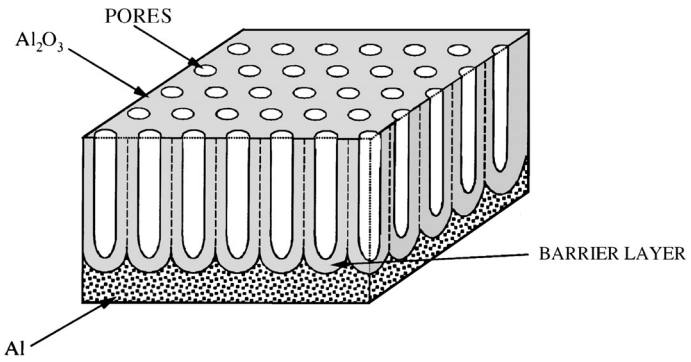

FIG. 1. Schematic of a porous anodic alumina template.

with a packing density on the order of 10^9 to $10^{11}/cm^2$ (Diggle *et al.,* 1969; O'Sullivan and Wood, 1970; AlMawlawi *et al.,* 1991; Zhang *et al.,* 1999). The film thickness (or pore length) ($< 1\ \mu$m to $> 50\ \mu$m) can be controlled by the duration of the anodization process. With their synthetic flexibility, ordered pore structure, high pore density, and high mechanical strength, anodic alumina systems have gained great popularity as a template material for nanowire fabrication. In addition, with recent improvements on the degree of pore ordering, anodic alumina has stimulated much interest for other device applications (Govyadinov and Zakhvitcevich, 1998; Davydov *et al.,* 1999; Li *et al.,* 1999; Masuda *et al.,* 1999; Li *et al.,* 2000; Kouklin *et al.,* 2000) because it provides a highly ordered two-dimensional nanopattern, readily and inexpensively, on a large scale compared to conventional lithographic approaches.

In the processing of anodic alumina films (Keller *et al.,* 1953; Masuda *et al.,* 1997; Li *et al.,* 1998a; Zhang *et al.,* 1999), a thin aluminum sheet is first mechanically and electrochemically polished to produce a smooth surface. It is then anodized in an acidic solution at a constant voltage and temperature. The anodization voltage V determines the interpore distance D by the empirical relation $D\,(\text{nm}) = -1.7 + 2.81{\cdot}V\,(\text{volts})$ (Li *et al.,* 1998a). Different electrolytes are usually used for different anodization voltage ranges: 20 wt% sulfuric acid (H_2SO_4) for less than 20 V, 4 wt% oxalic acid ($H_2C_2O_4$) for 30–65 V, and 3.5 wt% phosphoric acid (H_3PO_4) for 70 V or more. The as-prepared anodic alumina film has open pores on the top surface of the substrate and is capped by a barrier layer on the other side (see Fig. 1). Therefore, the sample has to be etched by an acidic solution to remove the barrier layer for suitable applications (Li *et al.,* 1998a; Jessensky *et al.,* 1998). Figures 2(a) and (b) show scanning electron microscopy (SEM) images of the top surfaces of porous alumina templates anodized in 4 wt% oxalic acid and 20 wt% sulfuric acid, respectively. The pore ordering and uniformity of these materials have been optimized by a two-step anodization technique (Li *et al.,* 1998b; Lin *et al.,* 2000).

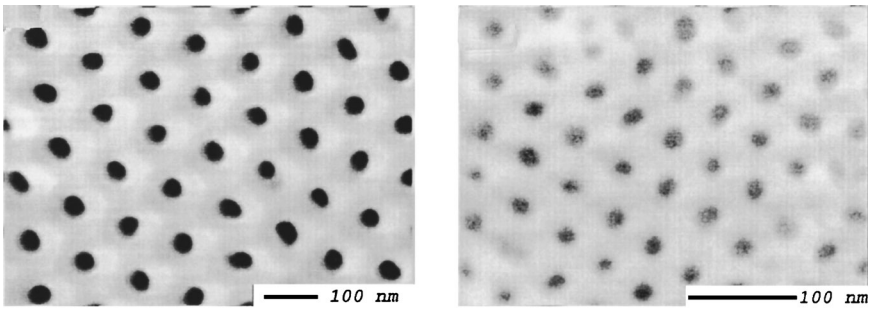

FIG. 2. SEM images of the top surfaces of porous anodic alumina templates anodized in (a) 4 wt% $H_2C_2O_4$ and (b) 20 wt% H_2SO_4. The average pore diameters in (a) and (b) are 44 nm and 18 nm, respectively.

The self-organized pore structure in anodic alumina is derived from two coupled processes, pore formation and pore ordering. Pore formation is generally believed to be a result of several mechanisms, including oxide formation and dissolution. During the anodization process, anions (O^{2-} or OH^-) migrate through the oxide layer and form Al_2O_3 at the oxide–metal interface, whereas some of the Al^{3+} ions produced at the oxide–metal interface move through the oxide layer and become ejected into the electrolyte. The nonuniform electric field and current density present in the sample from surface topological variations are essential to the pore growth mechanism. The surface variations may come from either the initial sample polishing or the self-induced variation during steady-state pore growth. The field-enhanced dissolution or the increased local temperature promotes the dissolution rate in some areas at the oxide-electrolyte interface to yield the observed pore morphology. The self-ordering of the pores may be attributed to the volume expansion during the oxide formation, which produces a repulsive force between the pores. In response to the mutual repulsive forces between neighboring pores, self-arrangements of the cylindrical pores will occur to maximize their packing density in the regular hexagonal order at steady state.

Porous templates can also be fabricated by chemically etching particle tracks originated from ion bombardment (Ferain and Legras, 1993; Sun *et al.,* 1999a). The pores produced by this track-etching method are randomly distributed with a packing density of 10^7 to $10^9/cm^2$, which is substantially lower than that in anodic alumina. By controlling the duration of chemical etching, the pore diameter can be varied from several hundred nanometers to about 5 nm. Track-etched polycarbonate membranes are commercially available in a variety of pore sizes and have been widely used in the template-assisted synthesis of nanowires (Martin, 1994; Blondel *et al.,* 1994; Liu *et al.,* 1998a).

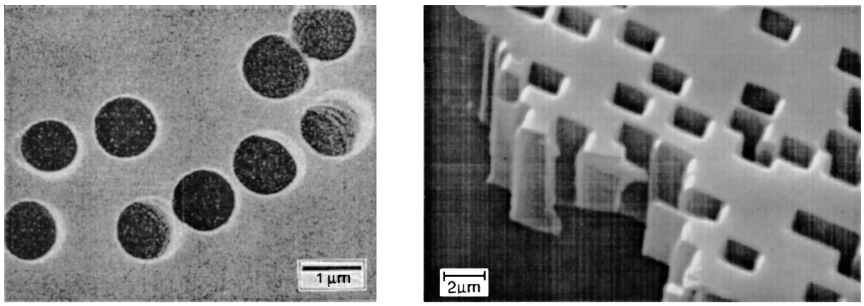

FIG. 3. (a) SEM image of the particle track-etched polycarbonate membrane, with a pore diameter of 1 μm (Martin, 1994). (b) SEM image of 2-μm pores in a single-crystal mica film prepared by particle track-etching (Sun *et al.,* 2000a).

Recently, single-crystalline mica films have also been used for the fabrication of track-etched pores (Sun *et al.,* 1999a). Polymer membranes have the disadvantage that they are relatively soft, so the definition of the pore morphology is not straightforward, and their internal pore surfaces can be quite rough. Also, they are fairly limited in working temperatures for sample fabrication and characterization compared to mica films, which are chemically stable up to 770 K. Figures 3(a) and (b) show the SEM images of etched tracks in polycarbonate membranes (Martin, 1994) and mica films (Sun *et al.,* 2000), respectively. The track-etched pores in the polymeric membranes are approximately cylindrical. Due to anisotropic etching rates, the pores in mica films have a diamond-shaped cross section with a tapered pore wall along the ion track (Sun *et al.,* 1999a).

Nanochannel glass (NCG) has also been proposed for the template-assisted synthesis of nanowires (Tonucci *et al.,* 1992; Huber *et al.,* 1994). It contains a regular hexagonal array of capillaries similar to the pore structure in anodic alumina. It is prepared by arranging two dissimilar glasses in a predetermined configuration. For example, Fig. 4(a) shows the use of cylindrical rods of an acid-etchable glass as the cores in a hexagonally packed matrix of inert glass tubes. The array of this core-tube assembly is then drawn at high temperatures to reduce the cross-sectional area. By repeating the drawing process, the channel diameters can be made as small as 33 nm, with a packing density of 3×10^{10} pores/cm^2 (Tonucci *et al.,* 1992). Finally, the core glass rods are etched away by an acid, yielding an array of cylindrical pores. Figure 4(b) shows a SEM micrograph of an NCG with 33-nm channels arranged in a hexagonal close packing (Tonucci *et al.,* 1992).

A number of other porous materials may be used as the host matrices for nanowire fabrication. A mesoporous molecular sieve termed MCM-41 (Beck *et al.,* 1992) possesses hexagonally packed pores with very small

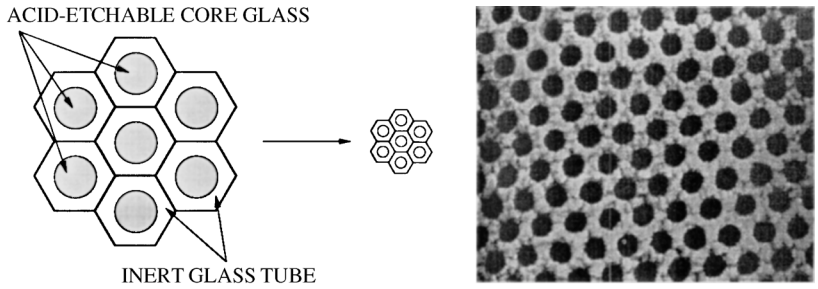

FIG. 4. (a) Schematic diagram illustrating the fabrication process for nanochannel glass array (Tonucci *et al.,* 1992). (b) SEM image of a glass array with 33-nm channels after acid etching (Tonucci *et al.,* 1992).

channel diameters, which can be systematically varied between 2 nm and 10 nm using a surfactant-based supramolecular template (Ying *et al.,* 1999). The surfactant molecule consists of a hydrophilic head group that has a high affinity for water and a long hydrophobic tail group. In the presence of water, surfactant species will undergo self-aggregation to form micellar structures, where the hydrophilic head groups are directed outward in contact with water, whereas the hydrophobic tail groups form the micellar core to minimize contact with water. Silicate precursors are then deposited on the ordered arrays of micelles, which are self-assembled at a high enough micellar concentration to form inorganic–organic mesostructures. The organic surfactants can be removed via heat treatment to yield silicates with hexagonally packed cylindrical pores. Wu and Bein (1994) have fabricated conducting organic filaments in the nanochannels of MCM-41. Han *et al.* (2000) have also prepared metallic nanowires in SBA-15 silica with hexagonally packed mesopores templated with triblock copolymers. Recently, the DNA molecule was also used as a template for growing nanometer-sized wires (Braun *et al.,* 1998).

The variety of porous solid materials that can be used as templates for nanostructure synthesis has been reviewed by Ozin (1992). In the template-assisted synthesis of nanowires, the pores or voids of the template are filled with the chosen material using a number of approaches. Nanowires have been derived via pressure injection, electrochemical deposition, and vapor deposition, as described in the following sections.

1. Pressure Injection

In the pressure injection method, the nanowires are formed by injecting the desired material in its liquid form into the pores of the template. This technique has been used to fabricate a number of metallic and

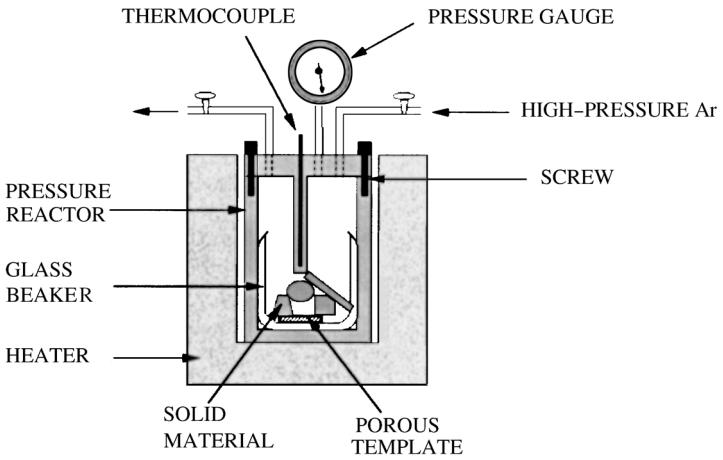

FIG. 5. Schematic of the experimental setup for the pressure injection of materials into the nanochannels of a porous template.

semiconducting nanowires (Huber *et al.,* 1994; Zhang *et al.,* 1998a; Lin *et al.,* 2000b). Before the injection process, the template is first cleaned to remove any particles or substances that may prevent the pores from being filled. The template is then placed with the solid material in a high-pressure chamber. The chamber is evacuated at a temperature slightly below the melting point of the solid material for a few hours to degas the template. It is then brought to a temperature above the melting point of the solid, so that the porous template is immersed in a liquid melt. Next, the chamber is disconnected from the vacuum system and filled with an inert gas such as argon. The high pressure within the chamber forces the liquid melt into the pores of the template. Following this pressure injection process, the chamber is slowly cooled to solidify the impregnated material within the nanochannels of the template before releasing the inert gas. By carefully controlling the cooling rate for nanowire solidification, it is possible to fabricate essentially single-crystalline wires (Zhang *et al.,* 1999). Figure 5 shows a schematic diagram of the experimental setup for the pressure injection process. The detailed pressure injection procedures are described by Huber *et al.* (1994) and Zhang *et al.* (1998a).

In the pressure injection process, a greater pressure is needed to overcome the surface tension for the liquid melt to enter pores of a smaller diameter. The relation between the pore diameter d_w and the required pressure P is given by the Washburn equation (Adamson, 1982),

$$d_W = -4\gamma \cos\theta / P, \tag{1}$$

where γ is the surface tension of the liquid and θ is the contact angle between the liquid and the template. For most liquid metals and semiconductors of interest, the surface tension ranges from 100 to 600 dyne/cm. Assuming the least favorable case of a nonwetting interface ($\theta = 180^\circ$) and a medium surface tension of 400 dyne/cm, filling channels 40 nm in diameter would require a pressure of about 400 bar. To reduce the pressure required or to maximize the filling factor, additives may be used to decrease the surface tension or the contact angle. For example, it was found that the introduction of a small quantity of copper atoms into the bismuth melt could facilitate the injection of liquid bismuth into porous anodic alumina (Zhang *et al.,* 1999).

For the pressure injection approach, the templates employed have to be chemically stable and structurally robust under the high pressures and temperatures involved. Anodic alumina and nanochannel glass can be used as template materials for this nanowire synthesis approach. Metallic (e.g. Bi, In, Sn and Al) and semiconducting (Se, Te, GaSb and Bi_2Te_3) nanowires have been pressure injected into anodic alumina templates (Huber *et al.,* 1994; Zhang *et al.,* 1998a; Lin *et al.,* 2000b). The following describes some of the important properties of bismuth nanowires fabricated by the pressure injection method.

Figure 6(a) shows a SEM image of bismuth nanowires embedded in an anodic alumina template after pressure injection. The pore diameter of the template was about 42 nm, and the maximum pressure and temperature applied for the injection process were about 310 bar and 325°C, respectively. A small amount of copper was introduced into liquid bismuth to enhance its injection; the copper atoms should be segregated from bismuth during solidification because they have zero solubility in solid bismuth. Upon solidification, the copper flakes were brought to the top surface of Bi due to their

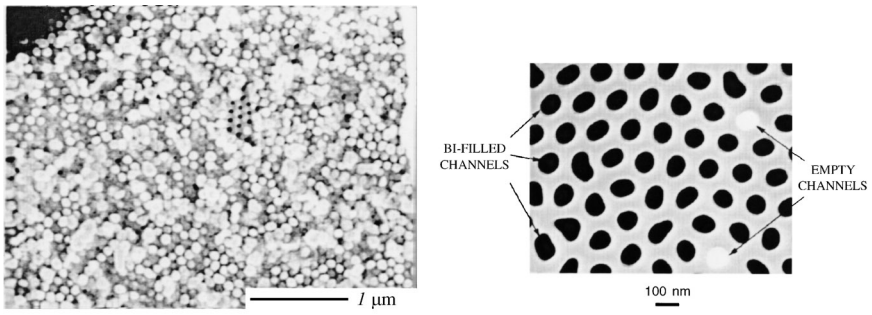

FIG. 6. (a) SEM image of the bottom surface of an anodic alumina template filled with bismuth. The pore diameter is 42 nm. (b) TEM micrograph of the cross section of a 65-nm bismuth nanowire array (Zhang *et al.,* 1999).

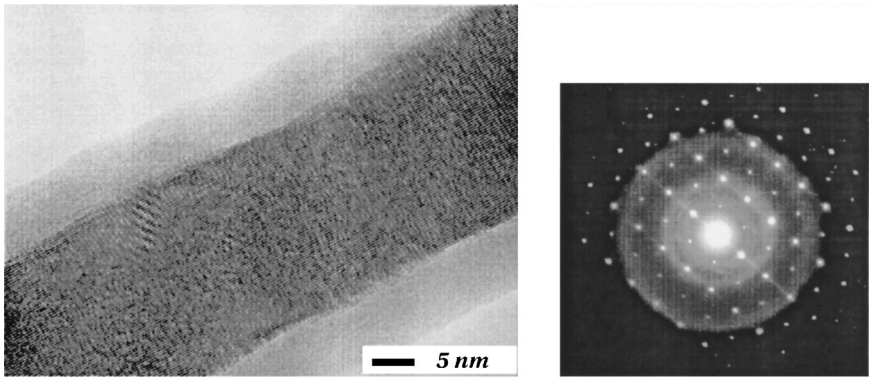

FIG. 7. (a) A HRTEM image of a 40-nm freestanding bismuth nanowire, showing lattice fringes. The amorphous surface layer is bismuth oxide formed upon air exposure of bismuth nanowire. (b) SAED pattern of a single Bi nanowire (Zhang *et al.,* 1999).

lower density, leaving pure bismuth nanowires within the pore channels. Figure 6(b) shows a TEM image of the cross section of a 65-nm Bi nanowire array, illustrating a high pore-filling factor (Zhang *et al.,* 1999). Because Bi has a higher electron density than anodic alumina, it is shown in dark contrast in the TEM image. Figure 7(a) shows a high-resolution transmission electron microscopy (HRTEM) image of a 40-nm freestanding bismuth nanowire, which was obtained by dissolving the anodic alumina template in a special acid solution that did not attack the bismuth nanowires. The freestanding wire was found to have a nearly uniform diameter (within 10%) along its length. The lattice fringes in Fig. 7(a) indicated a highly crystalline structure, as confirmed by the selected-area electron diffraction (SAED) pattern shown in Fig. 7(b). It was found that the alumina matrix protected the bismuth nanowires against oxidation, whereas freestanding wires were gradually oxidized upon exposure to air. The amorphous surface layer in Fig. 7(a) is the bismuth oxide developed when the nanowire was exposed to air prior to imaging.

Figure 8 shows X-ray diffraction (XRD) patterns of bismuth nanowire arrays (Lin *et al.,* 2000b). It illustrates that the crystal structure of bismuth nanowires is the same as that of bulk bismuth and that no copper phases were present. The nanowires have a preferred wire orientation dependent on their diameters. The major orientations of the 95-nm and 40-nm bismuth nanowire arrays were normal to the (202) and (012) lattice planes, respectively, indicating that most ($> 80\%$) of the nanowires were oriented along the $[10\bar{1}1]$ and $[01\bar{1}2]$ directions for $d_w \geq 60\,\text{nm}$ and $d_w \leq 50\,\text{nm}$, respectively (Zhang *et al.,* 1999; Lin *et al.,* 2000b). The existence of more than one dominant orientation in the 52-nm Bi nanowires (Fig. 8(b)) was

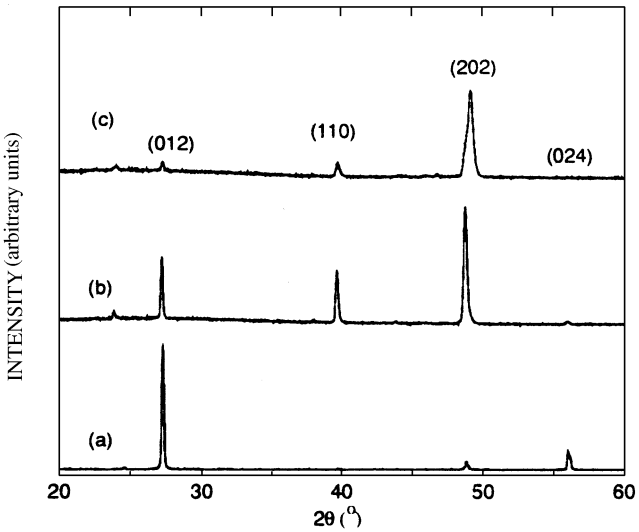

FIG. 8. XRD patterns of bismuth–anodic alumina nanocomposites with average bismuth wire diameters of (a) 40 nm, (b) 52 nm, and (c) 95 nm (Lin *et al.,* 2000b). The Miller indices corresponding to the lattice planes of bulk Bi are indicated above the individual peaks.

attributed to the transitional behavior of nanowires of 'intermediate' diameters as the preferential growth orientation was shifted from $[10\bar{1}1]$ to $[01\bar{1}2]$ with decreasing d_w. Huber *et al.* (2000) found a preferred crystal orientation [0001] along the wire axes for bismuth nanowires fabricated at a much higher pressure (about 1.5 kbar), indicating the possibility that the wire growth orientation might also depend on the applied pressure and other process parameters during the injection process. Additional XRD studies also revealed the presence of a metastable high-stress phase in the as-prepared bismuth nanowires (Zhang *et al.,* 1999), which could be converted to the normal phase by a thermal annealing treatment.

The smallest diameter attained for bismuth nanowires by the pressure injection method was about 13 nm, using a pressure of approximately 0.3 kbar (Zhang *et al.,* 1999). Finer nanowires might be fabricated by increasing injection pressures (Huber *et al.,* 2000), but it remains to be seen if the anodic alumina templates would retain their structural integrity under those high pressures.

2. Electrochemical Deposition

Electrochemical deposition has attracted increasing attention as a technique for nanowire fabrication. Traditionally, electrochemistry has been used to grow thin films on conducting surfaces. Because electrochemical

deposition is usually controllable in the direction normal to the substrate surface, this method can be readily extended to fabricate one-dimensional or zero-dimensional nanostructures if the deposition is confined within the pores of an appropriate template. The electrochemical technique involves first coating a thin conducting metal film onto one side of the porous membrane to serve as the cathode for electroplating. The length of the nanowires deposited can be controlled by the duration of the electroplating process. Electrochemical deposition has been used to synthesize nanowires and superlattices (Piraux *et al.,* 1994; Blondel *et al.,* 1994) of a variety of materials, including metals (e.g. Bi (Piraux *et al.,* 1999; Liu *et al.,* 1998a), Co (Ferre *et al.,* 1997; Zeng *et al.,* 2000), Fe (AlMawlawi *et al.,* 1991; Peng *et al.,* 2000), Ni (Ferre *et al.,* 1997; Sun *et al.,* 1999a), Cu (Piraux *et al.,* 1994; Blondel *et al.,* 1994), Ag (Bhattacharrya *et al.,* 2000), and Au (Hornyak *et al.,* 1997)), semiconductors (e.g., CdS (Routkevitch *et al.,* 1996a; Kouklin *et al.,* 2000)), superconductors (e.g., Pb (Yi and Schwarzacher, 1999)), and conducting polymers (Martin, 1994; Piraux *et al.,* 1999).

For electrochemical deposition, it is critical to choose a template system that is chemically stable in the electrolyte used and during the electrolysis process. The presence of cracks and defects in the templates will affect the electrochemical process, because deposition will occur predominantly in the more accessible cracks, leaving most of the nanochannels unfilled. Particle track-etched mica films or polymer membranes have been employed in simple dc electrolysis. To use anodic alumina in dc electrochemical deposition, the insulating barrier layer has to be removed first, and a metal film has to be evaporated onto one side of the template. However, the rectifying properties of the oxide barrier layer make it possible to use the ac deposition method directly. Although the applied voltage is sinusoidal and symmetrical, the current is greater during the cathodic half-cycles, so that deposition is dominant over the stripping that occurs in the subsequent anodic half-cycles. By retaining the barrier layer and using the ac electrolysis approach, the problem with cracks may be avoided, because there is no rectification at the defects, and the deposition process is reversed during each anodic half-cycle. By this approach, metals (e.g., Co (Zeng *et al.,* 2000) and Fe (AlMawlawi *et al.,* 1991; Peng *et al.,* 2000)) and semiconductors (e.g., CdS (Routkevitch *et al.,* 1996a; Kouklin *et al.,* 2000)) have been deposited within the pores of anodic alumina templates without removing the barrier layer.

In contrast to nanowires synthesized by the pressure injection method, nanowires derived electrochemically are typically polycrystalline with no preferred crystal orientation. However, some exceptions occur. For example, polycrystalline CdS nanowires fabricated by ac electrodeposition in anodic alumina were shown to have a preferred wire growth orientation along the c axis (Routkevitch *et al.,* 1996). Recently, Xu *et al.* (2000a, 2000b) prepared

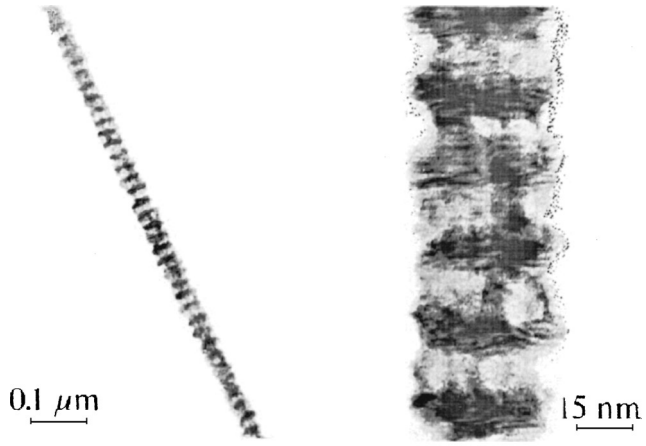

FIG. 9. (a) TEM image of a single Co(10 nm)/Cu(10 nm) multilayered nanowire. (b) A selected region of the sample at high magnification. (Piraux *et al.,* 1994.)

a number of single-crystalline nanowires of II–VI semiconductors (e.g., CdS, CdSe, and CdTe) in anodic alumina by dc electrodeposition in a nonaqueous electrolyte. Yi and Schwarzacher (1999) found that single-crystalline Pb nanowires can be formed by pulse electrodeposition under an overpotential, but no specific crystal orientation was noted along the wire axis.

One advantage of the electrochemical deposition technique is the possibility of fabricating multilayered structures within the nanowire systems. By varying the cathodic potentials in the electrolyte that contains two different kinds of ions, different metal layers are deposited controllably. Co–Cu multilayered nanowires have been synthesized to study the giant magnetoresistance (GMR) effect (Piraux *et al.,* 1994; Blondel *et al.,* 1994). Figure 9 shows TEM images of a single Co/Cu nanowire that is approximately 40 nm in diameter prepared by Piraux *et al.* (1994). The light bands represent Co-rich regions and the dark bands represent Cu-rich layers. This electrodeposition method provides a low-cost, effective approach for preparing multilayered one-dimensional nanostructures.

3. Vapor Deposition

Vapor deposition methods include physical vapor deposition (PVD) (Heremans *et al.,* 2000) and chemical vapor deposition (CVD) (Cheng *et al.,* 2000) or metallorganic chemical vapor deposition (MOCVD) (Berry *et al.,* 1996). Vapor deposition and electrochemical deposition are capable of

deriving nanowires of smaller diameters ($\leq$ 20 nm) more readily than pressure injection methods because they do not involve the use of high pressures to deposit materials inside the porous channels.

The experimental setup and procedures for the physical vapor deposition of bismuth nanowires are described by Heremans *et al.* (2000). The target material is placed in a crucible that is covered with the porous template to be filled. The template used for vapor deposition has open pores on both sides. The crucible, surrounded by heating wires, is inserted into a vacuum chamber. It is heated to melt the target material and to provide a high vapor pressure. Because the pressure outside is lower than that within the crucible, the vapor passes through the pores of the template. A slow cooling process is then initiated to produce a temperature gradient across the porous template. Because the temperature of the outer surface of the template is lower than that of the inner surface, the vapor begins to condense within the pores from the outer surface, and nanowires are grown inward. The process is completed once the temperature on the inner surface of the template falls below the melting point of the target material. Heremans *et al.* (2000) have synthesized nearly single-crystalline bismuth nanowires within anodic alumina by this approach; these nanowires possess a preferred crystal growth orientation along the wire axis, similar to that prepared by the pressure injection method (Zhang *et al.,* 1999; Heremans *et al.,* 2000).

Compound materials can also be prepared by the vapor deposition technique with two reacting gases (Cheng *et al.,* 2000). The reacting species with the lower melting point is placed in the crucible. The crucible, covered by the porous template, is inserted into a tube that contains the other reacting gas. The tube is heated up to vaporize the reactants in the crucible. The two gases then react to produce compound wires within the nanochannels of the template. Single-crystalline GaN nanowires have been synthesized in an anodic alumina template through reaction of Ga_2O vapor with a flowing ammonia stream (Cheng *et al.,* 1999, 2000). A different liquid/gas-phase approach has been used by Berry *et al.* (1996) to prepare polycrystalline GaAs and InAs nanowires in a nanochannel glass array. In this case, the nanochannels are filled with one liquid precursor (e.g., trimethyl gallium or triethyl indium) via a capillary effect, and the nanowires are formed by reaction between the liquid precursor and the gas reactant (e.g., AsH_3).

Recently, carbon nanotubes, an important class of one-dimensional nanostructures, have been fabricated within the pores of anodic alumina via CVD (Davydov *et al.,* 1999; Li *et al.,* 1999; Iwasaki *et al.,* 1999; Suh *et al.,* 1999). A small amount of metal (e.g., Co) is first electrochemically deposited on the bottom of the pores as a catalyst for the carbon nanotube growth, and the template is heated to 700 to 800°C in a flowing gas mixture of N_2 and acetylene or ethylene. The hydrocarbon molecules are then pyrolyzed to

form carbon nanotubes within the porous template. Using anodic alumina as the matrix, a highly ordered two-dimensional array of carbon nanotubes has been achieved. Such well-aligned nanotube array has stimulated much interest with its great potential for applications such as cold-cathode flat-panel displays.

B. Laser-Assisted Synthesis

In addition to the template-assisted method, laser-assisted synthesis has been developed for generating nanowires. It is particularly useful for producing large quantities of crystalline semiconducting nanowires with ultrafine diameters ($\leq$ 10 nm). Nanowire synthesis by the laser-assisted method is based on the vapor-liquid-solid (VLS) growth of single-crystalline silicon whiskers (Wagner and Ellis, 1964), which was discovered in the early 1960s. In VLS growth, a liquid metal droplet or catalyst cluster forms an energetically favored site for the adsorption of gas-phase reactants and the nucleation site for crystallization when supersaturated. The reactant crystallizes at the surface of the liquid cluster, and a preferentially one-dimensional structure is developed. Figure 10 shows a schematic of the silicon nanowire growth by the VLS mechanism. The one-dimensional structure obtained by such growth has a diameter larger than 0.1 μm, which is limited by the minimum size of the liquid droplet.

Recently, a laser ablation–condensation technique was used to produce nanometer-sized catalyst clusters to grow nanowires by the VLS method. A schematic of the laser ablation apparatus used by Morales and Lieber (1998) to produce silicon nanowires is shown in Fig. 11. The target consists of silicon and the catalyst material (e.g., $Si_{1-x}Fe_x$), and a pulsed laser is used to produce nanometer-sized catalyst clusters within a reaction chamber at 1200°C. The ablated materials are carried by an argon gas flow, and the

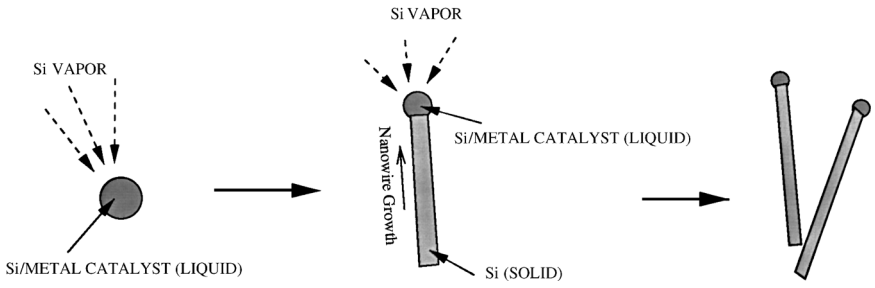

FIG. 10. Schematic illustrating the growth of silicon nanowires by the VLS mechanism.

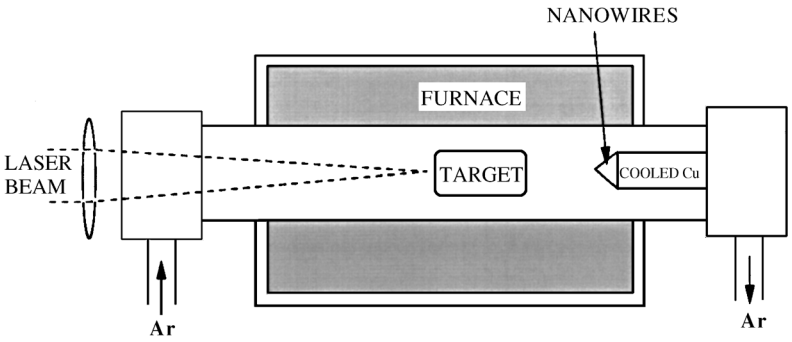

FIG. 11. Schematic of the laser ablation apparatus for the production of nanowires (Morales and Lieber, 1998).

nanowires generated are collected at the cold finger (Morales and Lieber, 1998; Lieber 1998). The growth of nanowires is affected by the reaction temperature and the catalyst material used (Morales and Lieber, 1998; Lieber, 1998; Duan and Lieber, 2000). It is believed that the nanowire growth occurs only when the catalyst cluster remains a liquid (Morales and Lieber, 1998). The wire growth ceases as the catalyst cluster is solidified when it is carried away from the hot zone of the furnace by the gas flow. All the nanowires are found to terminate at one end with catalyst clusters of diameters that are 1.5 to 2 times that of the wires. The nanowires range from 3 nm to tens of nanometers in diameter, with lengths up to tens of micrometers (Morales and Lieber, 1998; Duan and Lieber, 2000). Using the laser ablation technique, Lieber and coworkers have prepared a wide range of semiconducting nanowires, including group IV elements (Si and Ge), III–V compounds (GaAs, GaP, InAs, and InP), II–VI compounds (ZnS, ZnSe, CdS, and CdSe), and binary SiGe alloys (Morales and Lieber, 1998; Duan *et al.,* 2000; Duan and Lieber, 2000). Lee and coworkers also fabricated Si and Ge nanowires using a similar laser ablation apparatus (Zhang *et al.,* 1998b, 2000a).

Figure 12 shows TEM images of silicon nanowires fabricated by Morales and Lieber (1998). The nanowires are produced by laser ablating a $Si_{0.9}Fe_{0.1}$ target. In Fig. 12(a), the darker spheres with a diameter larger than the nanowires are the solidified $FeSi_2$ catalyst clusters that terminate at one end of the nanowires. Electron diffraction pattern indicates that the silicon nanowires are single-crystalline and grow along the [111] direction (Fig. 12(b)) (Morales and Lieber, 1998). The TEM image in Fig. 12(b) shows the silicon nanowire to be uniform in diameter, with a crystalline core that is surrounded by an oxide layer, which may have resulted from the presence of residual oxygen (Morales and Lieber, 1998; Duan *et al.,* 2000). Wang *et al.*

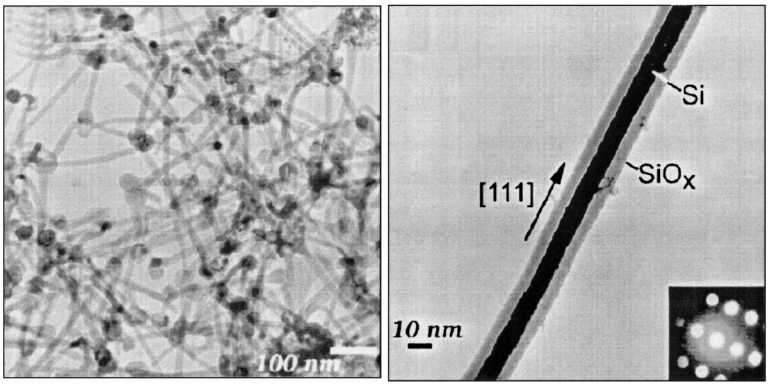

FIG. 12. (a) TEM images of Si nanowires produced after laser ablating a $Si_{0.9}Fe_{0.1}$ target. The dark spheres with a slightly larger diameter than the wires are solidified catalyst clusters (Morales and Lieber, 1998). (b) Diffraction contrast TEM image of a Si nanowire. The crystalline Si core appears darker than the amorphous oxide surface layer. The inset shows the convergent beam electron diffraction pattern recorded perpendicular to the wire axis (Morales and Lieber, 1998).

(1998a,b) found that these oxides played a more important role than metals in assisting the nanowire growth. SiO_x was discovered to be an effective catalyst that significantly increased the yield of silicon nanowires (Zhang *et al.,* 1998b; Wang *et al.,* 1998a, b). Similar yield enhancement was also found in the synthesis of germanium nanowires by laser ablating a germanium powder mixed with GeO_2 (Zhang *et al.,* 2000a). It was observed that targets composed of equal molar ratios of Ge:GeO_2 and Si:SiO_2 in the absence of metal catalysts gave the maximum yields for germanium and silicon nanowires, respectively (Zhang *et al.,* 2000a; Wang *et al.,* 1998a,b). Based on these observations and other TEM studies (Zhang *et al.,* 2000a; Wang *et al.,* 1998a; Lee *et al.,* 1999), an oxide-enhanced nanowire growth mechanism different from the classical VLS mechanism was proposed (Wang *et al.,* 1998a). It was postulated that the nanowire growth was catalyzed by the Ge_mO or Si_mO layer ($m > 1$) on the nanowire tips, which might be in or near their molten states (Lee *et al.,* 1999). Because the oxide-assisted laser ablation method did not require any metal catalysts, the resulting nanowires could achieve a high purity. The germanium and silicon nanowires produced from these catalyst-free targets were noted to grow generally along the [112] crystal direction (Lee *et al.,* 1999).

Although laser ablation methods have been used to fabricate large quantities of single-crystalline semiconducting nanowires with high aspect ratios, the wires obtained are randomly oriented with a variety of morphologies

(Tang *et al.,* 1999) and correspond to broad distributions of wire diameters and lengths. Therefore, it would be important to devote future research efforts toward controlling the wire diameter, length, morphology, and assembly in such synthesis in order to utilize the nanowires derived effectively for potential electronic applications.

C. Other Synthesis Methods

Recently, the VLS growth method has been extended beyond the gas-phase reaction to synthesis of Si nanowires in Si-containing solvent (Holmes *et al.,* 2000). In this case 2.5-nm Au nanocrystals were dispersed in supercritical hexane with a silicon precursor (e.g., diphenylsilane) under a pressure of 200–270 bar at 500°C, at which temperature the diphenylsilane decomposes to Si atoms. The Au nanocrystals serve as seeds for the Si nanowire growth, because they form an alloy with Si, which is in equilibrium with pure Si. It is suggested that the Si atoms would dissolve in the Au crystals until the saturation point is reached; then they are expelled from the particle to form a nanowire with a diameter similar to the catalyst particle. This method has an advantage over the laser-ablated Si nanowire in that the nanowire diameter can be well controlled by the Au particle size, whereas liquid metal droplets produced by the laser ablation process tend to exhibit a much broader size distribution. With this approach, highly crystalline Si nanowires with diameters ranging from 4 nm to 5 nm have been produced by Holmes *et al.* (2000). The crystal orientation of these Si nanowires can be controlled by the reaction pressure.

In addition to the fabrication methods discussed here, special techniques have been developed to prepare a variety of one-dimensional systems for investigating interesting quantum phenomena. For example, quantized conductance (in units of $G_0 = 2e^2/h$, where h is the Planck constant) has been observed through thin metallic nanowires with scanning tunneling microscopy (Pascual *et al.,* 1993, 1995; Brandbyge *et al.,* 1995) and mechanically controlled break junctions (Muller *et al.,* 1992, 1996). These techniques use the same basic principle of pressing two metals together and pulling them out to form a nanometer-sized wire between the two contacts. One-dimensional silicon nanostructures have also been fabricated on a silicon-on-insulator (SOI) substrate by a combination of lithography and orientation-dependent etching (Namatsu *et al.,* 1997). Other approaches include forming nanowires by vapor deposition on cleaved superlattice planes (Arakawa *et al.,* 1996) or by shadow deposition on stepped lattice planes (Sugawara *et al.,* 1997). These fabrication techniques usually require unique experimental configurations or complicated processing and produce nanowires with a very low yield or at a very high cost. Therefore, although the resulting nanostructures may be

helpful toward understanding low-dimensional phenomena, their utilization in commercial applications and devices is currently limited.

III. Theoretical Modeling of Nanowire Band Structures

Nanostructured materials exhibit behavior distinct from their bulk counterparts due to quantum confinement effects. As their length scale shrinks to a size comparable to the de Broglie wavelength of electrons, the energy of electrons in the confined direction becomes quantized and forms a discrete energy spectrum. If the separation between the quantized energy levels is much larger than the thermal excitation energy k_BT, virtually all the electrons will occupy the lowest possible states. Because it is not likely to promote electrons to a higher energy state in the absence of an external excitation, the degree of freedom for electrons is quenched in the confined direction, producing a system with reduced dimensionality. The systems confined in one, two, and three dimensions are treated as a two-dimensional (quantum well), a one-dimensional (quantum wire), and a zero-dimensional (quantum dot) electron gas, respectively. The energy quantization changes the band structure of nanostructured materials and alters their optical, magnetic, and electronic properties dramatically. Thus, the effects of quantum confinement on low-dimensional systems are of both fundamental and technological importance. In the following sections, a theoretical framework is presented for the modeling of one-dimensional nanowire systems. The Schrödinger equation has been solved to obtain the band structure of nanowires. Based on the band structure, a semiclassical model is developed to predict various transport properties of nanowire systems.

A. Band Structures of One-Dimensional Systems

The electronic states of nanowire systems exhibit a very different spectrum from that of bulk materials. In order to understand their unique electronic properties, we have modeled the band structure of these one-dimensional systems.

Without loss of generality, we assume a bulk material where the major carriers are electrons with an effective mass $\mathbf{m}_e$. In general, the electron masses are anisotropic, and the effective mass is expressed as a symmetric second-rank tensor. The dispersion relation of the electrons is written as

$$E(\mathbf{k}) = \frac{\hbar^2}{2}\mathbf{k} \cdot \boldsymbol{\alpha} \cdot \mathbf{k}, \tag{2}$$

where $\boldsymbol{k}$ is the wave vector and $\boldsymbol{\alpha}$ is the inverse tensor of $\mathbf{m}_e$. From the

effective mass theorem, the envelope wavefunction of electrons, $\psi(\mathbf{r})$, is described by the Schrödinger equation:

$$-\frac{\hbar^2}{2}\nabla\cdot\boldsymbol{\alpha}\cdot\nabla\psi(\mathbf{r}) = E\psi(\mathbf{r}). \tag{3}$$

For nanowires embedded in an insulating matrix with a large band gap (e.g., alumina or mica), electrons are well confined within the wires. Thus, to a good approximation, the electron wavefunction, $\psi(\mathbf{r})$, can be assumed to vanish at the wire boundary.

For an infinitely long wire with a circular cross section of diameter d_w, we take the z axis to be parallel to the wire axis, with the x and y axes lying on the cross-sectional plane. The cylindrical symmetry of the wire is then used to simplify Eq. (3) by making $\boldsymbol{\alpha}_{xy} = \boldsymbol{\alpha}_{yx} = 0$, which can be achieved by a proper rotation about the z axis. The wave function $\psi(\mathbf{r})$ then has the form

$$\psi(\mathbf{r}) = u(x, y)\exp(i\xi\cdot x)\exp(i\eta\cdot y)\exp(ik_z\cdot z), \tag{4}$$

where ξ and η are constants to be determined and k_z is the wave number of the traveling wave in the z direction. By letting $\xi = -(\alpha_{xz}/\alpha_{xx})k_z$ and $\eta = -(\alpha_{yz}/\alpha_{yy})k_z$, Eq. (3) is reduced to a concise second-order differential equation in x and y only:

$$-\frac{\hbar^2}{2}\left(\alpha_{xx}\frac{\partial^2}{\partial x^2} + \alpha_{yy}\frac{\partial^2}{\partial y^2}\right)u(x, y) = \left(E - \frac{\hbar^2 k_z^2}{2m_{zz}}\right)u(x, y), \tag{5}$$

where $m_{zz} = \hat{z}\cdot\mathbf{m}_e\cdot\hat{z}$ is the transport effective mass along the wire axis. Equation (5) is reminiscent of a two-dimensional Schrödinger equation with in-plane effective mass components

$$\begin{aligned} m_x &\equiv \alpha_{xx}^{-1} \\ m_y &\equiv \alpha_{yy}^{-1} \end{aligned} \tag{6}$$

in the x and y directions, respectively. Because $u(x, y)$ must satisfy the boundary condition: $u(x, y) = 0$ when $x^2 + y^2 = (d_w/2)^2$, the eigenvalues of $u(x, y)$ in Eq. (5) are quantized, and the energy of the electrons is written as

$$E_{nm}(k_z) = \varepsilon_{nm} + \frac{\hbar^2 k_z^2}{2m_{zz}}, \tag{7}$$

where ε_{nm} is the eigenvalue of Eq. (5) corresponding to the subband edge eigenstate at $k_z = 0$, labeled by the quantum numbers (n, m).

In a nanowire system, the quantized subband energy ε_{nm} and the transport effective mass m_{zz} along the wire axis are the two most important parameters and determine almost all the electronic properties. Due to the anisotropic carriers and the special geometric configuration (circular wire cross section and high aspect ratio of length to diameter), several approximations were used in earlier calculations to derive ε_{nm} and m_{zz} in bismuth nanowires. In the

first calculation carried out by Zhang *et al.* (1998c, 2000b), the quantized energy levels were evaluated by using a cyclotron effective mass approximation for the in-plane effective mass. An improved model was subsequently developed by Sun *et al.* (1999b) based on a square wire cross-section approximation, which allowed an analytical expression to be obtained for the wave functions. However, these two approximations were valid only for less anisotropic carriers, producing significant discrepancies for highly anisotropic systems ($\alpha_{xx}/\alpha_{yy} \gg 1$ or $\alpha_{xx}/\alpha_{yy} \ll 1$). Thus, a numerical approach was developed recently to more accurately determine ε_{nm} and m_{zz} (Lin *et al.,* 2000c).

For a simple case where $\alpha_{xx} = \alpha_{yy}$, the wave function of Eq. (5) has the analytical solution

$$u_{nm}(\mathbf{r}) \sim J_n(\chi_{nm} r) e^{\mathrm{i}n\theta}, \tag{8}$$

where J_n is the nth Bessel function and χ_{nm} is determined by the mth root of $J_n(x \cdot d_w/2) = 0$. The subband energy ε_{nm} corresponding to the wavefunction $u_{nm}(\mathbf{r})$ is given by

$$\varepsilon_{nm} = \frac{\hbar^2}{2} \alpha_{xx} \chi_{nm}^2. \tag{9}$$

For the general case where $\alpha_{xx} \neq \alpha_{yy}$, there are no analytical solutions, and the only possible approach to determine the quantized subband energy ε_{nm} from Eq. (5) is through numerical methods (Lin *et al.,* 2000c). In this instance, a mesh consisting of M concentric circles and N sectors is created within the wire cross section, as shown in Fig. 13. The differential equation of Eq. (5) is then transformed to a set of difference equations based on the grid points on

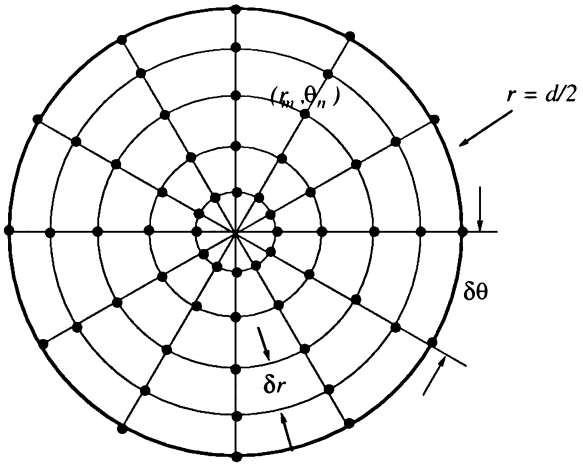

FIG. 13. Schematic of the grid points used to transform the differential equation into a difference equation. The mesh in the circular wire cross section consists of M concentric circles and N sectors. In this figure, $M = 5$ and $N = 12$ (Lin *et al.,* 2000c).

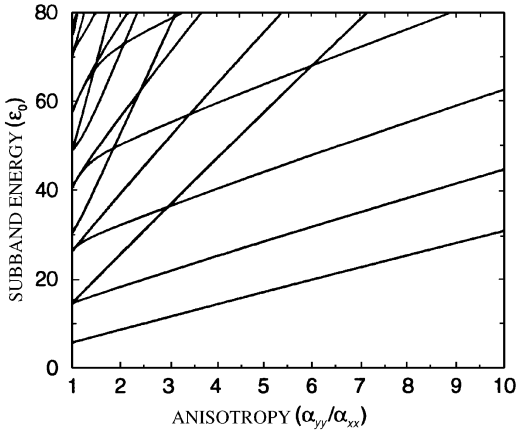

FIG. 14. Calculated subband energies in units of $\varepsilon_0 = 2\alpha_{xx}\hbar^2/d_w^2$ as a function of the in-plane mass anisotropy α_{yy}/α_{xx}. The subband energies of nanowires of various diameters can then be derived from this figure.

the mesh, which can be solved readily with the aid of computers. By refining the mesh, ε_{nm} can be obtained with great accuracy (within 0.1%). Figure 14 shows the calculated subband energies in units of $2\alpha_{xx}\hbar^2/d_w^2$ as a function of the mass anisotropy α_{yy}/α_{xx}.

The density of states (DOS) of electrons in nanowires is derived from Eq. (7) as

$$g(E) = \frac{\sqrt{2m_{zz}}}{\pi\hbar} \sum_{n,m} (E - \varepsilon_{nm})^{-1/2}. \tag{10}$$

Figure 15 shows the calculated DOS for electrons in a 40-nm bismuth nanowire compared to that of bulk bismuth. The DOS in nanowires is a superposition of one-dimensional transport channels, each located at a quantized subband energy ε_{nm}. We note that the DOS in nanowires has sharp peaks at the subband edges, whereas that in a bulk material is a smooth monotonic function of energy. The enhanced DOS at the subband edges of nanowires has important implications for many applications, such as in optics (Black *et al.,* 2000) and thermoelectrics (Hicks and Dresselhaus, 1993).

B. The Semimetal–Semiconductor Transition in Semimetallic Nanowires

For semimetals in bulk form, such as bismuth, the conduction band overlaps in energy with the valence band, and the electronic properties are

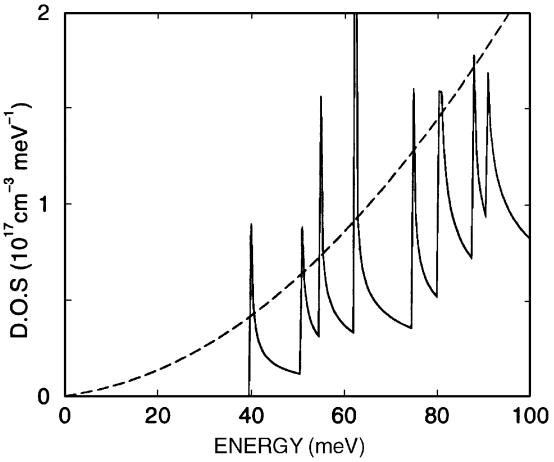

FIG. 15. Calculated effective densities of states for 40-nm bismuth nanowires (solid curve) and bulk bismuth (dashed curve). The zero energy refers to the band edge of bulk bismuth. The nonparabolic effects of the electron carriers are considered in these calculations.

governed by both the electrons and holes. In nanowires, the quantum confinement effects cause the band edge of the electrons to move up in energy (see Fig. 16), whereas the valence band edge decreases in energy. The band-edge energies of electrons and holes shift in opposite directions in bismuth nanowires, decreasing the energy overlap between the conduction band and the valence band (Fig. 16). As the wire diameter continues to decrease, the

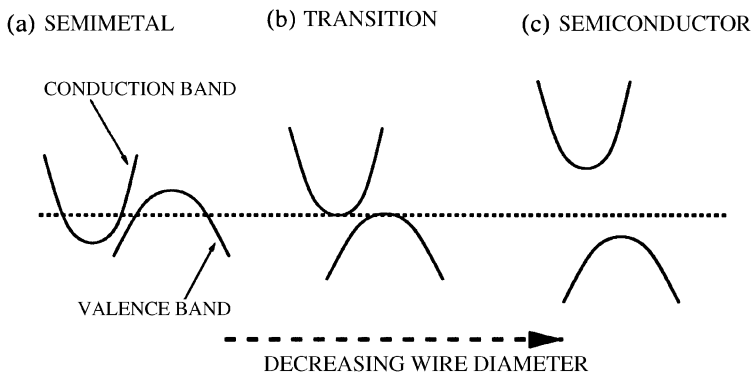

FIG. 16. Schematic illustrating the semimetal–semiconductor transition in nanowires made of semimetals: (a) bulk semimetals with a band overlap between the electrons and the holes, (b) nanowires with the critical wire diameter d_c where the band overlap vanishes, and (c) nanowires with diameters smaller than d_c, exhibiting a bandgap between the conduction and valence bands.

energy overlap eventually vanishes (Fig. 16(b)), producing a band gap between the lowest conduction subband and the highest valence subband. This semimetal-to-semiconductor transition will occur at a critical wire diameter d_c, which depends on the band overlap energy, the electron and hole effective masses, and the crystal orientation along the wire axis for the material of interest. The critical wire diameters for two group V semimetals, bismuth and antimony, are predicted to be about 50 nm and 10 nm (Lin *et al.,* 2000c; Heremans *et al.,* 2001), respectively. This quantum confinement–induced semimetal–semiconductor transition is one of the unique properties of nanowires made of semimetallic materials. Such a transition dramatically alters the electronic properties of nanowires, providing us with new possibilities for manipulating the band structures of materials.

Due to the semimetal–semiconductor transition, the carrier concentration $N(T)$ of nanowires made of semimetallic materials is highly dependent on the wire diameter and temperature and must satisfy the condition $d_w \leq d_c$ to exhibit semiconducting behavior. As an example, Fig. 17 shows the calculated total carrier densities for various bismuth nanowires oriented along the $[01\bar{1}2]$ growth direction as a function of temperature (Lin *et al.,* 2000c). Three different types of temperature dependence for the carrier density are predicted for bismuth nanowires, depending on the wire diameters. For 10-nm bismuth nanowires, which are in the semiconducting regime, the carrier density increases exponentially with temperature. For 80-nm bismuth nanowires, which remain in the semimetallic regime for all temperatures, the carrier density is similar in temperature dependence to bulk bismuth.

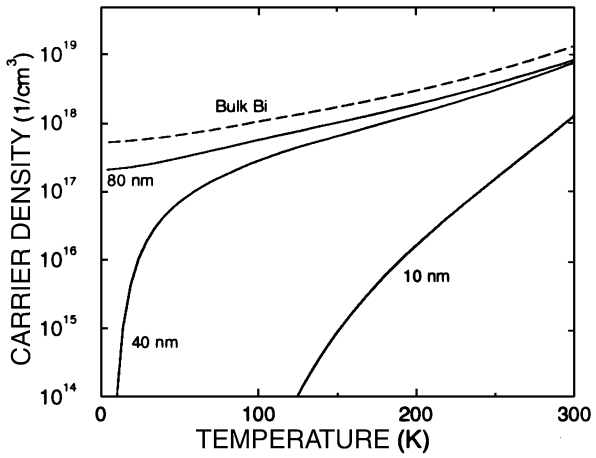

FIG. 17. Calculated total carrier density (electrons and holes) as a function of temperature for bulk 3D bismuth and bismuth nanowires of different diameters oriented along the $[01\bar{1}2]$ direction.

The lower carrier density of the 80-nm nanowires compared to bulk bismuth is due to the smaller band overlap in the former. For the 40-nm bismuth nanowires, the carrier density has a temperature dependence similar to bulk bismuth at high temperatures, but it drops rapidly with decreasing temperature at low temperatures. Because the carrier density is highly dependent on wire diameter, the transport properties of bismuth nanowires are expected to be highly sensitive to wire diameter, as will be shown experimentally in the section "temperature-dependent resistivity of nanowires."

IV. Transport Properties

The transport phenomena in low-dimensional systems can be roughly divided into two categories: ballistic transport and diffusive transport. Ballistic transport occurs when the electrons travel across a nanowire without any scattering. In this case, the conduction is determined mainly by the contacts between the nanowire and the external circuit, and the conductance is quantized into a universal conductance unit, $G_0 = 2e^2/h$ (Wharam *et al.,* 1988; van Wees *et al.,* 1988). Ballistic transport is usually observed in very short quantum wires, such as those produced by mechanically controlled break junctions (Muller *et al.,* 1992, 1996) or by scanning tunneling microscopy (Pascual *et al.,* 1993, 1995; Brandbyge *et al.,* 1995), whereby the wire length is much shorter than the electron mean free path and the conduction is a pure quantum phenomenon. An additional requirement for ballistic transport is that $k_B T \ll \varepsilon_j - \varepsilon_{j-1}$, where $\varepsilon_j - \varepsilon_{j-1}$ is the subband separation between the j and $j-1$ subband energy levels. On the other hand, for nanowires with lengths much longer than the carrier mean free path, the electrons or holes undergo numerous scattering events when they travel along the wire. In this case, electron transport is in the diffusive regime, and conduction is dominated by scattering due to phonons (lattice vibrations), boundary or lattice defects, and impurity atoms.

The ballistic transport of one-dimensional systems has been extensively studied since the discovery of quantized conductance (Wharam *et al.,* 1988; van Wees *et al.,* 1988). In contrast, due to the difficulty in fabricating long nanowires ($> 1\ \mu$m) and the inadequacy of conventional experimental techniques, there have been fewer experimental and theoretical studies on transport phenomena in the diffusive regime. Recently, a semiclassical transport model based on the band structure of nanowires was developed for systems in which scattering events are not negligible (Lin *et al.,* 2000b,c). The diffusive transport model has been applied to bismuth and antimony nanowire systems (Lin *et al.,* 2000b; Heremans *et al.,* 2001) and agrees well with the experimental findings.

A. Semiclassical Model

The diffusive transport phenomena in nanowires can be described by a semiclassical model based on the Boltzmann transport equation. For carriers in a one-dimensional subband, important transport coefficients, such as the electrical conductivity, σ, the Seebeck coefficient, S, and the thermal conductivity, κ_e, are derived as (Sun *et al.,* 1999b; Ashcroft and Mermin, 1976a)

$$\sigma = L^{(0)} \tag{11}$$

$$S = -\frac{1}{eT}\frac{L^{(1)}}{L^{(0)}} \tag{12}$$

$$\kappa_e = \frac{1}{e^2 T}\left(L^{(2)} - \frac{(L^{(1)})^2}{L^{(0)}}\right), \tag{13}$$

where T is temperature and

$$L^{(\alpha)} = e^2 \int \frac{4\,dk}{\pi^2 d_w^2}\left(-\frac{df}{dE}\right)\tau(k)v(k)v(k)(E(k) - E_f)^{\alpha}, \tag{14}$$

where $\alpha = 0, 1, 2$, k is the wave vector along the transport direction, $E(k)$ denotes the carrier dispersion relation, $v(k)$ is the group velocity, $\tau(k)$ is the relaxation time, E_f is the Fermi energy, and $f(E)$ is the Fermi–Dirac distribution function. Assuming a parabolic dispersion relation, the transport elements $L^{(\alpha)}$ in Eqs. (11)–(13) are derived as

$$L^{(0)} = D\left[\frac{1}{2}F_{-1/2}\right] \tag{15}$$

$$L^{(1)} = \begin{cases} (k_B T)D\left[\frac{3}{2}F_{1/2} - \frac{1}{2}\varsigma^* F_{-1/2}\right] & \text{(for electrons)} \\ -(k_B T)D\left[\frac{3}{2}F_{1/2} - \frac{1}{2}\varsigma^* F_{-1/2}\right] & \text{(for holes)} \end{cases} \tag{16}$$

$$L^{(2)} = (k_B T)^2 D\left[\frac{5}{2}F_{3/2} - 3\varsigma^* F_{1/2} + \frac{1}{2}\varsigma^{*2} F_{-1/2}\right], \tag{17}$$

where D is given by

$$D = \frac{8e}{\pi^2 d_w^2} = \left(\frac{2m^* k_B T}{\hbar^2}\right)^{1/2} \mu, \tag{18}$$

in which μ is the carrier mobility along the nanowire and

$$F_j = \int_0^{\infty} \frac{x^j\,dx}{\exp(x - \varsigma^*) + 1} \tag{19}$$

denotes the Fermi–Dirac related functions, with fractional indices. $j = -\frac{1}{2}$, $\frac{1}{2}$, $\frac{3}{2}$. The reduced chemical potential, ς^*, is defined as

$$\varsigma^* = \begin{cases} \left(E_f - \varepsilon_e^{(0)}\right)/k_B T & \text{(for electrons)} \\ \left(\varepsilon_h^{(0)} - E_f\right)/k_B T & \text{(for holes),} \end{cases} \tag{20}$$

where $\varepsilon_e^{(0)}$ and $\varepsilon_h^{(0)}$ denote the band edges for electrons and holes, respectively. In considering the transport properties of real one-dimensional nanowires, contributions from all the subbands near the Fermi energy should be included, and the $L^{(\alpha)}$s in Eqs. (11)–(13) should be replaced by the sum of contributions from each subband i, $L_{total}^{(\alpha)} = \sum_i L_i^{(\alpha)}$, to obtain the various transport coefficients.

It should be noted that the carrier mobility in nanowires is lower than that in bulk single-crystalline material due to possible scattering at wire and grain boundaries, uncontrolled impurities, and lattice defects. The overall effect of this additional scattering is taken into account by Matthiessen's rule (Ashcroft and Mermin, 1976b),

$$\frac{1}{\mu_{\text{tot}}(T)} = \frac{1}{\mu_{\text{bulk}}(T)} + \frac{1}{\mu_{\text{bound}}} + \frac{1}{\mu_{\text{imp}}(T)}, \tag{21}$$

where μ_{bulk} is the carrier mobility in bulk crystalline material and the terms μ_{bound}^{-1} and μ_{imp}^{-1} account for boundary scattering and charged impurity scattering, respectively. Also, μ_{bound}^{-1} is usually assumed to be independent of temperature, whereas μ_{imp}^{-1} has a temperature dependence of $T^{1.5}$ for most charged impurity scattering processes.

B. Temperature-Dependent Resistivity of Nanowires

A number of transport measurements have been performed on nanowires prepared by the template-assisted approach. The nanowire-embedded template provides a convenient package for making electrical contacts on both ends of the wires, so that two-point transport measurements can be performed. Transport properties of various nanowire arrays have been measured by Zhang *et al.* (1998c, 2000b), Heremans *et al.* (1998, 2000), Liu *et al.* (1998b), Huber *et al.* (1999), Hong *et al.* (1999), Lin *et al.* (2000b), and Sun *et al.* (2000). Although a two-point resistance measurement has the advantage of simplicity, an absolute resistivity value for the nanowires cannot be determined by this approach, because the number of wires in the template contributing to the conduction measurement is not known. Progress was recently made to characterize the absolute resistivity of a single nanowire

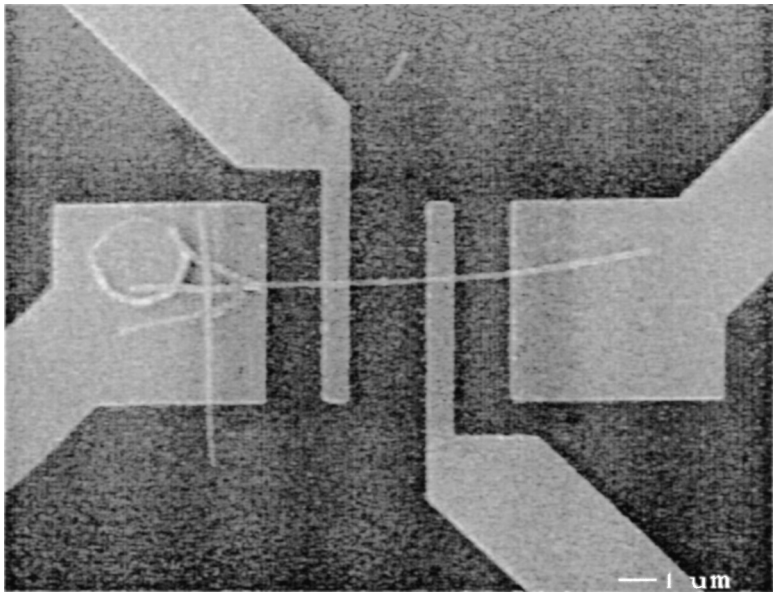

FIG. 18. SEM image of a 70-nm bismuth nanowire with four electrodes attached to the nanowire. The circle on the large left electrode is a reference point used to find the nanowire and to attach electrodes to it by a lithographic process (Cronin *et al.,* 1999).

via a four-point setup (Cronin *et al.,* 1999, 2000), which could provide more physical information on the properties of nanowires than the normalized resistance of a nanowire array. Figure 18 shows an SEM image of a four-point electrode patterned on a 70-nm Bi nanowire (Cronin *et al.,* 1999). The circular dot in Fig. 18 represents one of the prepatterned grid points used to locate the nanowires on the substrate. In this case, nanoelectrodes were patterned by electron-beam lithography on top of a single nanowire on a substrate coated with a thin insulating layer (Cronin *et al.,* 1999, 2000). The electrodes consisted of a gold layer ($\sim$ 1000 Å thick) and a thin adhesive layer, and their processing followed a standard *lift-off* method. We note that most nanowires would undergo surface oxidation upon removal from the template. The surface oxide layer on the nanowires imposes a serious problem in making nanoelectrical contacts; efforts are currently being devoted to tackling this challenge.

Figure 19(a) shows the temperature dependence of resistance $R(T)$ for bismuth nanowire arrays ($d_w = 7 - 200$ nm) synthesized by vapor deposition and measured by Heremans *et al.* (2000). Hong *et al.* (1999) reported similar resistance measurements on bismuth wires of larger diameters (200 nm to 2 μm) prepared by electrochemical deposition (Fig. 19(b)). These two studies

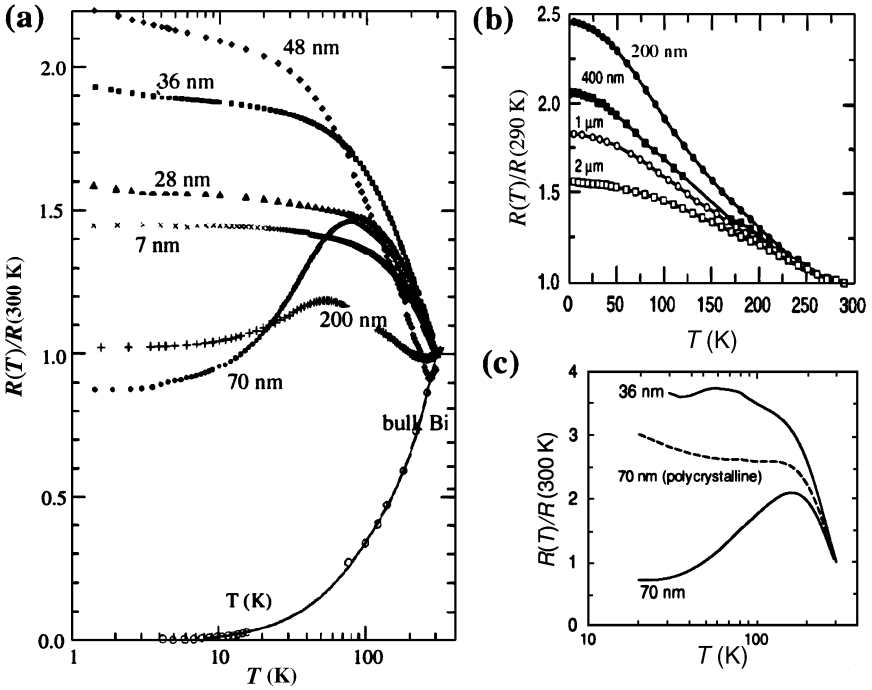

FIG. 19. (a) Measured temperature dependence of resistance for bismuth nanowire arrays of various wire diameters d_w (Heremans *et al.,* 2000). (b) $R(T)/R(290\,K)$ for bismuth wires of larger d_w measured by Hong *et al.* (1999). (c) Calculated $R(T)/R(300\,K)$ of 36-nm and 70-nm bismuth nanowires (Lin *et al.,* 2000b). The dashed curve refers to a 70-nm polycrystalline wire with increased boundary scattering.

showed that $R(T)$ of nanowires is highly sensitive to d_w and is very different from that of bulk bismuth. In Fig. 19(a), the temperature dependence of resistance for bismuth nanowires exhibits dissimilar trends for $d_w > 50$ nm and $d_w \leq 50$ nm. Based on the semiclassical transport model and the band-structure model of bismuth nanowires, $R(T)/R(300\text{ K})$ was calculated for 36-nm and 70-nm wires. The two wire diameters were chosen to represent semiconducting and semimetallic bismuth nanowires, respectively. The solid curves in Fig. 19(c) (Lin *et al.,* 2000b) illustrate that the calculated $R(T)/R(300\text{ K})$ trends are consistent with those obtained experimentally (Fig. 19(a)). We note that the nonmonotonic $R(T)$ behavior for semimetallic nanowires observed by Heremans *et al.,* 2000 in Fig. 19(a) is not found in the wires of Fig. 19(b). This inconsistency may be due to the crystal quality differences in the bismuth wires prepared by the two different approaches, which can be accounted for by μ_{bound} in the transport model. Instead of the nonmonotonic behavior exhibited by single-crystalline semimetallic nanowires in Fig. 19(a),

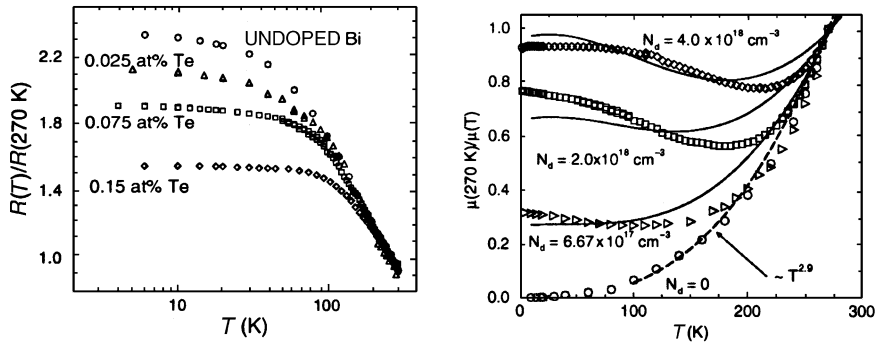

FIG. 20. (a) Measured $R(T)/R(270\,K)$ for 40-nm bismuth nanowires prepared with alloys of different Te doping levels. (b) The calculated temperature dependence of μ_{avg}^{-1} for 40-nm undoped and Te-doped bismuth nanowires of different N_d. The dashed and solid lines are fitting curves corresponding to undoped and Te-doped Bi nanowires, respectively.

$R(T)$ is predicted to display a monotonic temperature dependence at a high defect level. This is illustrated by the dashed curve in Fig. 19(c) for polycrystalline 70-nm bismuth wires. Because the nanowires prepared by electrochemical deposition were found to be polycrystalline, their carriers would experience more boundary scattering, resulting in the monotonic $R(T)$ behavior noted experimentally in Fig. 19(b).

The same transport model has also been extended to describe the properties of Te-doped bismuth nanowires and antimony nanowires. Te, a group VI element, is an electron donor in bismuth. Figure 20(a) shows the measured $R(T)/R(270\text{ K})$ for 40-nm Bi nanowires with the Te concentrations used to form the Bi–Te alloys for nanowire synthesis. The actual Te concentrations in the bismuth nanowires would be smaller than these nominal values because some Te atoms would segregate to the wire boundary during alloy solidification (Zhang *et al.,* 2000b). For simplicity, we assume that about 10% of the Te dopants in the alloy melt are present in the final nanowire product and that each Te atom donates one electron to the conduction band of bismuth. Therefore, 0.025, 0.075, and 0.15 at% Te-doped Bi alloys give rise to donor concentrations N_d of 6.67×10^{17}, 2.0×10^{18}, and 4.0×10^{18} cm^{-3} in the respective nanowires. Based on the measured $R(T)$ in Fig. 20(a) and the calculated temperature-dependent carrier density, the average carrier mobility, $\mu_{\text{avg}}(T)$, of the Te-doped bismuth nanowires can be obtained. Analogous to Eq. (21), μ_{avg}^{-1} for doped bismuth nanowires can be related to the various scattering processes by $\mu_{\text{doped}}^{-1}(T) = \mu_{\text{undoped}}^{-1}(T) + \mu_{\text{imp}}^{-1}(T) + \mu_{\text{defect}}^{-1}$, where μ_{undoped} is the average mobility of the undoped bismuth nanowires with the same diameter and μ_{imp}^{-1} and μ_{defect}^{-1} are associated with the increased ionized impurity scattering and the higher defect level in Te-doped

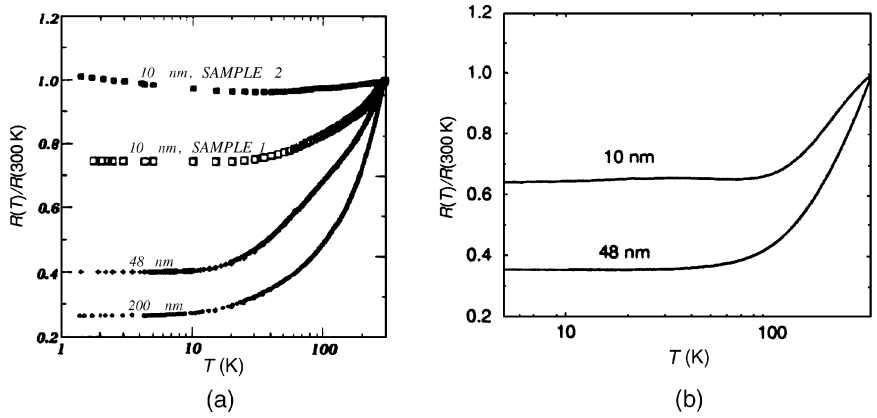

FIG. 21. (a) Temperature dependence of the resistance measured for various antimony nanowires, normalized to the resistance at 300 K. (b) Calculated $R(T)/R(300\,K)$ for 10-nm and 48-nm antimony nanowires.

bismuth nanowires, respectively. The $\mu_{\text{avg}}{}^{-1}(T)$ values calculated are shown in Fig. 20(b) as solid curves, which are qualitatively consistent with the experimental results (denoted by symbols).

Like bismuth, antimony is semimetallic in bulk form. The band overlap between electrons and holes in antimony is about 180 meV at 4 K, which is about five times larger than that in bismuth ($\sim$ 38 meV). Therefore, the semimetal–semiconductor transition would occur at a smaller wire diameter in antimony nanowires ($\sim$ 10 nm) compared to bismuth nanowires ($\sim$ 50 nm). Figure 21(a) shows the temperature dependence of the resistance for antimony nanowires prepared by vapor deposition (Heremans *et al.,* 2001). One of the 10-nm nanowire arrays has less resistance variation with temperature than the other, probably due to differences in impurity content or wire diameter distribution within the anodic alumina templates. Figure 21(b) illustrates the modeled $R(T)$ curves for 10-nm and 48-nm antimony nanowire arrays, which display trends that are qualitatively consistent with the experimental results shown in Fig. 21(a) (Heremans *et al.,* 2001). The fact that the measured $R(T)$ of antimony and bismuth nanowires can be explained by the same transport model suggests that the different temperature dependences of the resistance between nanowires and bulk materials arise from both quantum finite-size effects and classical finite-size effects. The classical finite-size effect decreases the carrier mobility by limiting the carrier mean free path, whereas the quantum confinement effect alters the band structure (especially for semimetals) and significantly changes the carrier density. Together, these two factors determine the temperature dependence of resistance in the nanowire systems. Finite-size effects in nanowires have also been observed in the

magnetoresistance measurements of bismuth and nickel nanowire arrays (Fasol, 1998; Sun *et al.,* 2000).

V. Summary

Recent developments in the fabrication of nanowires have led to significant advances in research on these low-dimensional systems. The laser-assisted synthesis has successfully produced a variety of semiconducting nanowires with ultrafine diameters. In contrast, most metallic nanowires have been prepared in a regular array with a well-controlled wire-packing geometry via the template-assisted approach. Nanoporous templates provide a useful matrix for handling nanowires and for device integration. The semimetallic nanowires of bismuth and antimony have been shown to undergo a transition to semiconducting behavior with decreasing wire diameters. A generalized theoretical framework has been developed to predict the band structure and transport properties of nanowire systems. Theoretical calculations indicate that nanowires exhibit a very different band structure from that of their bulk counterparts, resulting in unusual optical, electronic and thermoelectric properties. Transport studies suggest that quantum confinement effects significantly perturb the carrier density, whereas the carrier mean free path is limited mainly by the wire diameter. Consequently, transport phenomena in nanowire systems can be manipulated by tuning the diameter of these one-dimensional structures.

Nanowire systems present a great challenge for the understanding and utilization of low-dimensional materials. Although device fabrication based on nanowire systems is still in its infancy, these nanostructures have demonstrated a significant potential for technological breakthroughs with their unique band structure and transport properties. They offer tremendous research opportunities at the frontiers of nanotechnology. Future advances in this field would entail further interdisciplinary efforts toward developing novel synthesis method and control of self-assembled nanostructures, detailed understanding and theoretical modeling of quantum confinement effects, and sophisticated characterization of nanostructures with high aspect ratios.

ACKNOWLEDGMENTS

The authors acknowledge helpful discussions with Dr. Z. Zhang, Dr. G. Dresselhaus, Dr. J. Heremans, O. Rabin, M. R. Black, and S. B. Cronin. They are grateful to the NSF, the U.S. Navy, the MURI program, and DARPA for financial support.

REFERENCES

Adamson, A. W., "Physical Chemistry of Surfaces." Wiley, New York, 1982, p. 338.

AlMawlawi, D., Coombs, N., and Moskovits, M., Magnetic properties of Fe deposited into anodic aluminum-oxide pores as a function of particle size. *J. Appl. Phys.* **70,** 4421 (1991).

Arakawa, T., Watabe, H., Nagamune, Y., and Arakawa, Y., Fabrication and microscopic photoluminescence imaging of ridge-type InGaAs quantum wires grown on a (110) cleaved plane of AlGaAs/GaAs superlattice. *Appl. Phys. Lett.* **69,** 1294 (1996).

Ashcroft, N. W., and Mermin, N. D., "Solid State Physics." Holt, Rinehart and Winston, New York, 1976a, Chap. 13.

Ashcroft, N. W., and Mermin, N. D., "Solid State Physics." Holt, Rinehart and Winston, New York, 1976b, Chap. 16.

Beck, J. S., Vartuli, J. C., Roth, W. J., Leonowicz, M. E., Kresge, C. T., Schmitt, K. D., Chu, C. T-W., Olson, D. H., Sheppard, E. W., McCullen, S. B., Higgins, J. B., and Schlenker, J. L., A new family of mesoporous molecular sieves prepared with liquid crystal templates. *J. Am. Chem. Soc.* **114,** 10834 (1992).

Berry, A. D., Tonucci, R. J., and Fatemi, M., Fabrication of GaAs and InAs wires in nanochannel glass. *Appl. Phys. Lett.* **69,** 2846 (1996).

Bhattacharrya, S., and Saha, S. K., Nanowire formation in a polymeric film. *Appl. Phys. Lett.* **76,** 3896 (2000).

Black, M. R., Lin, Y.-M., Dresselhaus, M. S., Tachibama, M., Fang, S., Rabin, O., Ragot, F., Eklund, P. C., and Dunn, B., Measuring the dielectric properties of nanostructures using optical reflection and transmission: bismuth nanowires in porous alumina. *MRS Symp. Proc.* **581,** 623 (2000).

Blondel, A., Meier, J. P., Doudin, B., and Ansermet, J.-Ph., Giant magnetoresistance of nanowires of multilayers. *Appl. Phys. Lett.* **65,** 3019 (1994).

Brandbyge, M., Schiøtz, J., Sörensen, M. R., Stoltze, P., Jacobsen, K. W., Nørskov, J. K., Olesen, L., Laegsgaard, E., Stensgaard, I., and Besenbacher, F., Quantized conductance in atom-sized wires between two metals. *Phys. Rev. B* **52,** 8499 (1995).

Braun, E., Eichen, Y., Sivan, U., and Ben-Yoseph, G., DNA-templated assembly and electrode attachment of a conducting silver wire. *Nature* **391,** 775 (1998).

Cheng, G. S., Zhang, L. D., Zhu, Y., Fei, G. T., Li, L., Mo, C. M., and Mao, Y. Q., Ordered nanostructure of single-crystalline GaN nanowires in a honeycomb structure of anodic alumina. *Appl. Phys. Lett.* **75,** 2455 (1999).

Cheng, G. S., Zhang, L. D., Chen, S. H., Li, Y., Li, L., Zhu, X. G., Zhu, Y., Fei, G. T., and Mao, Y. Q., Ordered nanostructure of single-crystalline GaN nanowires in a honeycomb structure of anodic alumina. *J. Mater. Res.* **15,** 347 (2000).

Chou, S. Y., Krauss, P. R., and Kong, L. S., Nanolithograpically defined magnetic structures and quantum magnetic disk. *J. Appl. Phys.* **79,** 6101 (1996).

Cronin, S. B., Lin, Y.-M., Koga, T., Sun, X., Ying, J. Y., and Dresselhaus, M. S., Thermoelectric investigation of bismuth nanowires, *in* "The 18th International Conference on Thermoelectrics: ICT Symposium Proceedings" (G. Chen, Ed.), p. 554. IEEE, Piscataway, NJ, 1999.

Cronin, S. B., Lin, Y.-M., Koga, T., Ying, J. Y., and Dresselhaus, M. S., Transport measurements of individual bismuth nanowires. *MRS Symp. Proc.* **582,** 10.4 (2000).

Davydov, D. N., Sattari, P. A., AlMawlawi, D., Osika, A., and Haslett, T. L., Field emitters based on porous aluminum oxide templates. *J. Appl. Phys.* **86,** 3983 (1999).

Diggle, J. W., Downie, T. C., and Goulding, C. W., Anodic oxide films on aluminum. *Chem. Rev.* **69,** 365 (1969).

Duan, X., and Lieber, C. M., General synthesis of compound semiconductor nanowires. *Adv. Mater.* **12,** 298 (2000).

Duan, X., Wang, J., and Lieber, C. M., Synthesis and optical properties of gallium arsenide nanowires. *Appl. Phys. Lett.* **76,** 1116 (2000).

Fasol, G., Nanowires: Small is beautiful. *Science* **280,** 545 (1998).

Ferain, E., and Legras, R., Track-etched membrane-dynamics of pore formation. *Nucl. Instrum. Methods B* **84,** 539 (1993).

Ferre, R., Ounadjela, K., George, J. M., Piraux, L., and Dubois, S., Magnetization processes in nickel and cobalt electrodeposited nanowires. *Phys. Rev. B* **56,** 14066 (1997).

Foss, C. A., Jr., Tierney, M. J., and Martin, C. R., Template synthesis of infrared-transparent metal microcylinders—comparison of optical properties with the predictions of effective medium theory. *J. Phys. Chem.* **96,** 9001 (1992).

Govyadinov, A. N., and Zakhvitcevich, S. A., Field emitter arrays based on natural self-organized porous anodic alumina. *J. Vac. Sci. Technol. B* **16,** 1222 (1998).

Han, Y.-J., Kim, J. M., and Stucky, G. D., Preparation of noble metal nanowires using hexagonal mesoporous silica SBA-15. *Chem. Mater.* **12,** 2068 (2000).

Heremans, J., Thrush, C. M., Zhang, Z., Sun, X., Dresselhaus, M. S., Ying, J. Y., and Morelli, D. T., Magnetoresistance of bismuth nanowire arrays: a possible transition from 1D to 3D localization. *Phys. Rev. B* **58,** R10091 (1998).

Heremans, J., Thrush, C. M., Lin, Y.-M., Cronin, S. B., Zhang, Z., Dresselhaus, M. S., and Mansfield, J. F., Bismuth nanowire arrays: Synthesis and galvanomagnetic properties. *Phys. Rev. B* **61,** 2921 (2000).

Heremans, J., Thrush, C. M., Lin, Y.-M., Cronin, S., and Dresselhaus, M. S., Transport properties of antimony nanowires. *Phys. Rev. B.* **63,** 5406 (2001).

Hicks, L. D., and Dresselhaus, M. S., Thermoelectric figure of merit of a one-dimensional conductor. *Phys. Rev. B* **47,** 16631 (1993).

Holmes, J. D., Johnston, K. P., Doty, R. C., and Korgel, B. A., Control of thickness and orientation of solution-grown silicon nanowires. *Science* **287,** 1471 (2000).

Hong, K., Yang, F. Y., Liu, K., Reich, D. H., Searson, P. C., and Chien, C. L., Giant positive magnetoresistance of Bi nano wire arrays in high magnetic fields. *J. Appl. Phys.* **85,** 6184 (1999).

Hornyak, G. L., Patrissi, C. J., and Martin, C. R., Fabrication, characterization, and optical properties of gold nanoparticle/porous alumina composites: the nonscattering Maxwell-Garnett. *J. Phys. Chem.* **101,** 1548 (1997).

Huber, C. A., Huber, T. E., Sadoqi, M., Lubin, J. A., Manalis, S., and C. B., Prater, Nanowire array composites. *Science* **263,** 800 (1994).

Huber, T. E., Graf, M. J., and Foss, C. A., Jr., Low contact resistance 30 nm and 200 nm diameter Bi wire array composites, *in* "The 18th International Conference on Thermoelectrics: ICT Symposium Proceedings" (G. Chen, Ed.), p. 558. IEEE, Piscataway, NJ, 1999.

Huber, T. E., Graf, M. J., Foss, C. A., Jr., and Constant, P., Processing and characterization of high-conductance bismuth wire array composites. *J. Mater. Res.* **15,** 1816 (2000).

Iwasaki, T., Motoi, T., and Den, T., Mutiwalled carbon nanotubes growth in anodic alumina nanoholes. *Appl. Phys. Lett.* **75,** 2044 (1999).

Jessensky, O., Müller, F., and Gösele, U., Self-organized formation of hexagonal pore arrays in anodic alumina. *Appl. Phys. Lett.* **72,** 1173 (1998).

Keller, F., Hunter, M. S., and Robinson, D. L., Structural features of oxide coating on aluminum. *J. Electrochem. Soc.* **100,** 411 (1953).

Kouklin, N., Bandyopadhyay, S., Tereshin, S., Varfolomeev, A., and Zaretsky, D., Electronic bistability in electrochemically self-assembled quantum dots: A potential nonvolatile random access memory. *Appl. Phys. Lett.* **76,** 460 (2000).

Lee, S. T., Zhang, Y. F., Wang, N., Tang, Y. H., Bello, I., Lee, C. S., and Chung, Y. W., Semiconductor nanowires from oxides. *J. Mater. Res.* **14,** 4503 (1999).

Li, A. P., Müller, F., Birner, A., Neilsch, K., and Gösele, U., Hexagonal pore arrays with a 50–420 nm interpore distance formed by self-organization in anodic alumina. *J. Appl. Phys.* **84,** 6023 (1998a).

Li, F., Zhang, L., and Metzger, R. M., On the growth of highly ordered pores in anodized aluminum oxide. *Chem. Mater.* **10,** 2470 (1998b).

Li, J., Papadopoulos, C., Xu, J. M., and Moskovits, M., Highly ordered carbon nanotube arrays for electronic applications. *Appl. Phys. Lett.* **75,** 367 (1999).

Li, Y., Holland, E. R., and Wilshaw, P. R., Synthesis of high density arrays of nanoscaled gridded field emitters based on anodic alumina. *J. Vac. Sci. Technol. B* **18,** 994 (2000).

Lieber, C. M., One-dimensional nanostructures: chemistry, physics and applications. *Solid State Commun.* **107,** 607 (1998).

Lin, Y.-M., Sun, X., Cronin, S. B., Zhang, Z., Ying, J. Y., and Dresselhaus, M. S., Fabrication and transport properties of Te-doped bismuth nanowire arrays. *MRS Symp. Proc.* **582,** 10.3 (2000a).

Lin, Y.-M., Cronin, S. B., Ying, J. Y., Dresselhaus, M. S., and Heremans, J. P., Transport properties of Bi nanowire arrays. *Appl. Phys. Lett.* **76,** 3944 (2000b).

Lin, Y.-M., Sun, X., and Dresselhaus, M. S., Investigation of thermoelectric transport properties of cylindrical Bi nanowires. *Phys. Rev. B* **62,** 4610 (2000c).

Liu, K., Chien, C. L., Searson, P. C., and Kui, Y. Z., Structural and magneto-transport properties of electrodeposited bismuth nanowires. *Appl. Phys. Lett.* **73,** 1436 (1998a).

Liu, K., Chien, C. L., and Searson, P. C., Finite-size effects in bismuth nanowires. *Phys. Rev. B* **58,** 14681 (1998b).

Martin, C. R., Nanomaterials: A membrane-based synthetic approach. *Science* **266,** 1961 (1994).

Masuda, H., Yamada, H., Satoh, M., Asoh, H., Nakao, M., and Tamamura, T., Highly ordered nanochannel-array architecture in anodic alumina. *Appl. Phys. Lett.* **71,** 2772 (1997).

Masuda, H., Ohya, M., Asoh, H., and Nakao, M., Photonic crystal using anodic porous alumina. *Jpn. J. Appl. Phys.* **38,** 1403 (1999).

Morales, A. M., and Lieber, C. M., A laser ablation method for the synthesis of crystalline semiconductor nanowires. *Science* **279,** 208 (1998).

Muller, C. J., van Ruitenbeek, J. M., and de Jongh, L. J., Conductance and supercurrent discontinuities in atomic-scale metallic constrictions of variable width. *Phys. Rev. Lett.* **69,** 140 (1992).

Muller, C. J., Krans, J. M., Todorov, T. N., and Reed, M. A., Quantization effects in the conductance of metallic contacts at room temperature. *Phys. Rev. B* **53,** 1022 (1996).

Namatsu, H., Horiguchi, S., Nagase, M., and Kurihara, K., Fabrication of one-dimensional nanowire structures utilizing crystallographic orientation in silicon and their conductance characteristics. *J. Vac. Sci. Technol. B* **15,** 1688 (1997).

Nötzel, R., Ledentsov, N. N., Daweeritz, L., and Ploog, K., Semiconductor quantum-wire structures directly grown on high-index surfaces. *Phys. Rev. B* **45,** 3507 (1992).

Omi, H., and Ogino, T., Self-assembled Ge nanowires grown on Si(113). *Appl. Phys. Lett.* **71,** 2163 (1997).

O'Sullivan, J. P., and Wood, G. C., The morphology and mechanism of formation of porous anodic films on aluminum. *Proc. Royal Soc. London A* **317,** 511 (1970).

Ozin, G. A., Nanochemistry: synthesis in diminishing dimensions. *Adv. Mater.* **4,** 612 (1992).

Pascual, J. I., Mendez, J., Gómez-Herrero, J., Baró, A. M., Garcia, N., and Binh, V. T., Quantum contact in gold nanostructures by scanning tunneling microscopy. *Phys. Rev. Lett.* **71,** 1852 (1993).

Pascual, J. I., Mendez, J., Gómez-Herrero, J., Baró, A. M., Garcia, N., Landman, U., Luedtke, W. D., Bogachek, E. N., and Cheng, H. P., Properties of metallic nanowires—from conductance quantization to localization. *Science* **267,** 1793 (1995).

Peng, Y., Zhang, H.-L., Pan, S.-L, and Li, H.-L., Magnetic properties and magnetization reversal of α-Fe nanowires. *J. Appl. Phys.* **87,** 7405 (2000).

Piraux, L., George, I. M., Despres, J. F., Leroy, C., Ferain, E., Legras, R., Ounadjela, K., and Fert, A., Giant magnetoresistance in magnetic multilayered nanowires. *Appl. Phys. Lett.* **65,** 2484 (1994).

Piraux, L., Dubois, S., Duvail, J. L., and Radulescu, A., Fabrication and properties of organic and metal nanocylinders in nanoporous membranes. *J. Mater. Res.* **14,** 3042 (1999).

Routkevitch, D., Bigioni, T., Moskovits, M., and Xu, J. M., Electrochemical fabrication of CdS nanowire arrays in porous anodic aluminum oxide templates. *J. Phys. Chem.* **100,** 14307 (1996a).

Routkevitch, D., Tager, A. A., Haruyama, J., AlMawlawi, D., Moskovits, M., and Xu, J. M., Nonlithographic nanowire arrays: Fabrication, physics, and device applications. *IEEE Trans. Electron. Dev.* **43,** 1646 (1996b).

Sugawara, A., Coyle, T., Hembree, G. G., and Scheinfein, M. R., Self-organized Fe nanowire arrays prepared by shadow deposition on NaCl(110) template. *Appl. Phys. Lett.* **70,** 1043 (1997).

Suh, J. S., and Lee, J. S., Highly ordered two-dimensional carbon nanotube arrays. *Appl. Phys. Lett.* **75,** 2047 (1999).

Sun, L., Searson, P. C., and Chien, C. L., Electrochemical deposition of nickel nanowire arrays in single-crystal mica films. *Appl. Phys. Lett.* **74,** 2803 (1999a).

Sun, X., Zhang, Z., and Dresselhaus, M. S., Theoretical modeling of thermoelectricity in bismuth nanowires. *Appl. Phys. Lett.* **74,** 4005 (1999b).

Sun, L., Searson, P. C., and Chien, C. L., Finite-size effects in nickel nanowire arrays. *Phys. Rev. B* **61,** R6463 (2000).

Tang, Y. H., Wang, N., Zhang, Y. F., Lee, C. S., Bello, I., and Lee, S. T., Synthesis and characterization of amorphous carbon nanowires. *Appl. Phys. Lett.* **75,** 2921 (1999).

Tonucci, R. J., Justus, B. J., Campillo, A. J., and Ford, C. E., Nanochannel array glass. *Science* **258,** 783 (1992).

van Wees, B. J., van Houten, H., Beenakker, C. W. J., Williamson, J. G., Kouwenhoven, L. P., van der Marel, D., and Foxon, C. T., Quantized conductance of point contacts in a two-dimensional electron gas. *Phys. Rev. Lett.* **60,** 848 (1988).

Wagner, R. S., and Ellis, W. C., Nanowire formation in a polymeric film. *Appl. Phys. Lett.* **4,** 89 (1964).

Wang, N., Tang, Y. H., Zhang, Y. F., Lee, C. S., and Lee, S. T., Nucleation and growth of Si nanowires from silicon oxide. *Phys. Rev. B* **58,** R16024 (1998a).

Wang, N., Zhang, Y. F., Tang, Y. H., Lee, C. S., and Lee, S. T., SiO_2-enhanced synthesis of Si nanowires by laser ablation. *Appl. Phys. Lett.* **73,** 3902 (1998b).

Wharam, D. A., Thornton, T. J., Newbury, R., Pepper, M., Ahmed, H., Frost, J. E. F., Hasko, D. G., Peacock, D. C., Ritchie, D. A., and Jones, G. A. C., One-dimensional transport and the quantization of the ballistic resistance. *J. Phys. C* **21,** L209 (1988).

Whitney, T. M., Jiang, J. S., Searson, P. C., and Chien, C. L., Fabrication and magnetic-properties of arrays of metallic nanowires. *Science* **261,** 1316 (1993).

Wu, C.-G., and Bein, T., Conducting polyaniline filaments in a mesoporous channel host. *Science* **264,** 1757 (1994).

Xu, D., Chen, D., Xu, Y., Shi, X., Guo, G., Gui, L., and Tang, Y., Preparation of II–VI group semiconductor nanowire arrays by dc electrochemical deposition in porous aluminum oxide templates. *Pure Appl. Chem.* **72,** 127 (2000a).

Xu, D., Xu, Y., Chen, D., Guo, G., Gui, L., and Tang, Y., Preparation of CdS single-crystal nanowires by electrochemically induced deposition. *Adv. Mater.* **12,** 520 (2000b).

Yi, G., and Schwarzacher, W., Single crystal superconductor nanowires by electrodeposition. *Appl. Phys. Lett.* **74,** 1746 (1999).

Ying, J. Y., Nanoporous systems and templates: The unique self-assembly and synthesis of nanostructures. *Science Spectra* **18,** 56 (1999).

Ying, J. Y., Mehnert, C. P., and Wong, M. S., Synthesis and applications of supramolecular-templated mesoporous materials. *Angew. Chem. Int. Ed.* **38,** 56 (1999).

Yu, D. P., Lee, C. S., Bello, I., Zhou, G. W., and Bai, Z. G., Synthesis of nano-scale silicon wires by excimer laser ablation at high temperature. *Solid State Commun.* **105,** 403 (1998).

Zeng, H., Zheng, M., Skomski, R., Sellmyer, D. J., Liu, Y., Menon, L., and Bandyopadhyay, S., Magnetic properties of self-assembled Co nanowires of varying length and diameter. *J. Appl. Phys.* **87,** 4718 (2000).

Zhang, Z., Ying, J. Y., and Dresselhaus, M. S., Bismuth quantum-wire arrays fabricated by a vacuum melting and pressure injection process. *J. Mater. Res.* **13,** 1745 (1998a).

Zhang, Y. F., Tang, Y. H., Wang, N., Yu, D. P., Lee, C. S., Bello, I., and Lee, S. T., Silicon nanowires prepared by laser ablation at high temperature. *Appl. Phys. Lett.* **72,** 1835 (1998b).

Zhang, Z., Sun, X., Dresselhaus, M. S., Ying, J. Y., and Heremans, J., Magnetotransport investigation of ultrafine single-crystalline bismuth nanowire arrays. *Appl. Phys. Lett.* **73,** 1589 (1998c).

Zhang, Z., Gekhtman, D., Dresselhaus, M. S., and Ying, J. Y., Processing and characterization of single-crystalline ultrafine bismuth nanowires. *Chem. Mater.* **11,** 1659 (1999).

Zhang, Y. F., Tang, Y. H., Wang, N., Lee, C. S., Bello, I., and Lee, S. T., Synthesis and characterization of amorphous carbon nanowires. *Phys. Rev. B* **61,** 4518 (2000a).

Zhang, Z., Sun, X., Dresselhaus, M. S., Ying, J. Y., and Heremans, J., Electronic transport properties of single crystal bismuth nanowire arrays. *Phys. Rev. B* **61,** 4850 (2000b).